Chapter 8

MUON COLLIDER RING

Contents

8.1 Introduction 326

8.2 Lattice 327

8.2.1 Overview 328

8.2.2 Components of the Lattice 330

8.2.3 Performance 334

8.2.4 Control of the Momentum Compaction 336

8.2.5 Collider lattice comparisons 338

8.2.6 Summary 339

8.3 Superconducting Magnets 340

8.3.1 Energy Deposition Due to Muon Decay 341

8.3.2 Collider Ring Dipoles 342

8.3.3 Collider Ring Quadrupoles and Sextupoles 343

8.3.4 Reduction of Heat Load in SC magnets 344

8.4 Radio-Frequency System for the Collider Ring 347

8.5 Ring Vacuum Chamber 350

8.5.1 Particle Fluxes 350

8.5.2 Beam Gas Scattering and Beam Tube Gas Density Requirement . 353

8.5.3 Sources of Beam Tube Gas and Estimate of Beam Tube Gas Density 354

8.5.4 Beam Tube Resistivity and Image Current Losses 355

8.6 Classical Beam-Beam Interaction 355

8.6.1 Introduction. 356
8.6.2 Physics of the Incoherent Simulation. 357
8.6.3 Beam-beam Simulation. 358
8.6.4 Other Classical Beam-Beam Issues. 363
8.6.5 Summary 366
8.7 QED Effects at the Interaction Region 367
8.8 Single Bunch Collective Effects 370

8.1 Introduction

The collider ring of the Muon Complex allows for (about) 1000 collisions per bunch, rather than the single collision that is possible in a linear collider geometry. If the transverse beam size at the collision point in a muon collider were the same as that in an electron-positron linear collider, there would be a full increase in luminosity of order 1000. This is not the case. The muon bunch is cooled as much as possible, but still has an emittance that is significantly larger than the extremely low emittances required in an electron-positron linear collider. The luminosity scales as $L = fN^2/((\epsilon_x\beta_x^*)(\epsilon_y\beta_y^*))^{1/2}$, where $\epsilon_{x(y)}$ is the beam emittance in the $x(y)$ phase plane, $\beta_{x(y)}^*$ the corresponding beta-function at the interaction point (which is limited, by the hour-glass effect, to be no less than the bunch length), and f the collision frequency.

While the NLC electron-positron linear collider and the muon collider are quite different, in particular this muon collider feasibility study is for a 4 TeV (center of mass) machine and the NLC energy range is .5-1.5 TeV, it is instructive to compare the parameters that are required for achieving the design luminosity. For typical NLC parameters: $f = 18,000 = 100 \times 180$ (bunches per pulse $\times$ pulses per second), $N = 10^{10}$, $\epsilon_{nx} = 5 \times 10^{-6}$m, $\beta_x^* = 10^{-2}$m, $\epsilon_{ny} = 5 \times 10^{-8}$m, $\beta_y^* = 10^{-4}$m for a luminosity of $7 \times 10^{33}\text{cm}^{-2}\text{s}^{-1}$ at $250\,\text{GeV} \times 250\,\text{GeV}$.

In contrast, the muon collider has $f = 30,000Hz = 2 \times 1000 \times 15$ (bunch pairs/pulse $\times$ collisions/bunch-pair $\times$ pulses/second), $N = 2\times10^{12}$, a round beam with $\epsilon_n = 5\times10^{-5}$mrad, $\beta^* = 3\times10^{-3}$ m, for a luminosity of $10^{35}\text{cm}^{-2}\text{s}^{-1}$ at 2 TeV $\times$ 2 TeV. Thus, the muon collider achieves its luminosity primarily with an increased number of particles (and from an increased number of collisions per bunch-pair). The muon collider has a much larger emittance and beam size at the IP ($\sigma_x\sigma_y|_{NLC} \approx 10^{-15}\text{m}^2$, while $\sigma_x\sigma_y|_{muon} \approx 10^{-12}\text{m}^2$). The large emittance may relax some tolerances on component alignment compared to electron-positron linear colliders, but these bunch parameters, coupled with the need to store ~ 1000 turns, present many difficulties.

The ring design is challenging, with its high current, low beta, and isochronicity requirements. The low beta and high current are required to obtain the luminosity, and the isochronicity is required to maintain the short bunch length without excessive rf. Luminosity cannot be further increased by reducing the muon bunch length, for the bunch length is determined by longitudinal cooling, which is, already, as much as can be done. For the very high charge one must be concerned with collective instabilities and wakefields.

The ring brings many technical complications to the project (as well as cost, not addressed herein), but we we have an ideas on how each can be handled, and advocate further investigation of a collider ring that achieves the very high luminosity requisite for operation at high energy.

This chapter examines the design and analysis of various systems envisioned for the muon collider main ring. This work includes magnet designs, lattice design, vacuum requirements, analysis of collective instabilities, and beam-beam interaction. First lattice studies are presented (Section 8.2), and then the superconducting magnets, both dipoles and quadrupoles (Section 8.3). In Section 8.4 we consider the ring rf system. Section 8.5 is devoted to the vacuum chamber which require special care as it must absorb the energy of decay electrons and their synchrotron radiation. The classical beam-beam interaction, incoherent and coherent, are covered in the next section (Section 8.6). Incoherent pair production is covered in Sec. 8.7. Finally, in Section 8.8, collective effects are discussed. The major parameters of the muon collider are presented in Table 8.1.

8.2 Lattice

The lattice for a 2-TeV on 2-TeV muon collider must satisfy three major design constraints. The first and most difficult of these is provision of an Interaction Region (IR) with an extremely low β^* (~ 3 mm) consistent with an acceptable dynamic aperture. Second, the ring must exhibit a high degree of isochronicity in order to preserve short 3 mm long bunches with a modest rf system. Lastly, there must be small corrected chromaticity, so that the momentum-dependent tune spread of the beam fits between resonances. Technically, considerable shielding must be incorporated into the design to protect the superconducting magnets from the high muon-decay backgrounds. The following sections describe a preliminary lattice, Ref. [1], which is intended to meet the above requirements.

Table 8.1: High energy-high luminosity $\mu^+\,\mu^-$ collider

Maximum c-m Energy [TeV]	4
Luminosity $\mathcal{L}[10^{35}\mathrm{cm}^{-2}\mathrm{s}^{-1}]$	1.0
Circumference [km]	8.08
Time Between Collisions [μs]	12
Energy Spread σ_E[units 10^{-3}]	2
Pulse length σ_z[mm]	3
Free space at the IP [m]	6.25
Luminosity life time [No.turns]	900
Horizontal betatron tune, ν_x	55.79
Vertical betatron tune, ν_y	38.82
rms emittance, $\epsilon_{x,y}$ [μm-rad]	0.0026
rms normalized emittance, $\gamma\epsilon_{x,y}$ [μm-rad]	50.0
Beta-function values at IP, $\beta^*_{x,y}$ [mm]	3
rms Beam size at IP [μm]	2.8
Quadrupole pole fields near IP [T]	6.0
Peak beta-function, $\beta_{x\mathrm{max}}$ [km]	284
Peak beta-function, $\beta_{y\mathrm{max}}$ [km]	373
Magnet Aperture closest to IP [cm]	12
Beam-Beam tune shift per crossing	0.05
Repetition Rate [Hz]	15
rf frequency [GHz]	1.3
rf voltage [MeV]	130
Particles per Bunch [units 10^{12}]	2
No. of Bunches of each sign	2
Peak current $\mathcal{I} = eNc/\sqrt{2\pi}\sigma_z$ [kA]	12.8
Average current $\mathcal{I} = eNc/$Circum [A]	0.032

8.2.1 Overview

To obtain the design luminosity, considering the projected muon production rate, requires very low β-function values at the IP, $\beta^* = 3\,\mathrm{mm}$. Additionally, the *hour-glass* effect requires bunch lengths comparable to β^*. Maintaining such short bunches with moderate rf voltages requires a momentum compaction factor of 10^{-6} or less. (Just to preserve the bunch length for one turn requires $|\alpha| \ll \sigma_z/C\delta \simeq 10^{-4}$, where C is the circumference.) These are the major challenges of the muon collider lattice design. Studies addressing these issues have

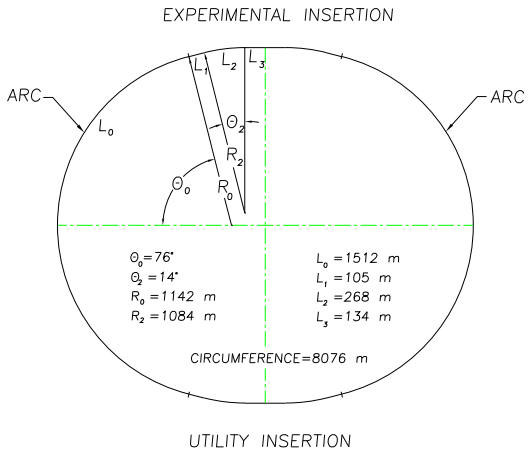

Figure 8.1: The complete collider ring layout.

been recently published [2].

The very small β^* requirement is particularly difficult to achieve because substantial space must be reserved for the detector about the IP and also because the superconducting magnets must be shielded from the decay products of the muon beam. In the initial design, superconducting quadrupoles nearest the IP had to accommodate a 6 cm thick tungsten liner in order to dissipate heat generated by the beam. Recent work has been successful in reducing the required shielding to 2 cm using combinations of sweep dipoles and collimators. With the thicker liner, quadrupole gradients were reduced by about a factor of 4 near the IP. However, with the thinner liner, the strength reduction will be factor of 2, since the beam size and liner thickness will be comparable. Additionally, a magnet-free length of ± 6.5 m must be reserved about the IP to provide the ± 150 mr acceptance angle needed for the detector. As a result, peak beta-function values as high as several hundred kilometers cannot be avoided; these high values produce extremely large chromaticities (several thousand before correction).

One preliminary design of an entire collider ring has been developed using the experimental insertion and arc modules described in Ref.[2]-[4] plus a utility insertion. A schematic layout of this ring design is shown in Fig. 8.1. A second collider ring design, has been developed by K. Oide[4]. This design incorporates a more sophisticated nonlinear correction scheme in the IR. Unfortunately, because of time constraints, it was impossible to include an equal discussion of the two designs here. Therefore, we will proceed with a detailed presentation of the first design, to be followed by a section comparing the two designs, and, finally, a discussion of recent progress.

8.2.2 Components of the Lattice

The ring has an oval shape, with reflection symmetry about two perpendicular axes, see Fig. 8.1. The lattice has two nearly circular 152° arcs joined by two insertions, each containing two 14° bending sections. These are called the experimental and utility insertions.

The two arcs are identical; each contains 22 periods and one dispersion suppressor at each end. The insertions are geometrically identical; each is symmetric about its center. Each half insertion has three parts: two straight sections separated by a bending section. The bending sections are identical in the experimental and utility insertions, except for the sextupole strengths. In contrast, the straight parts have different quadrupole lengths and gradients in the two insertions. Thus, as a focusing structure the ring has one superperiod with reflection symmetry about the line joining the centers of the two insertions.

Arc module In order to have very short 3 mm bunches in the 2 TeV muon collider, the storage ring must be quasi-isochronous, which requires that the momentum compaction α be very close to zero[9], where α is defined in terms of offsets of the momentum p and equilibrium orbit circumference C by

$$\alpha(p) = \frac{p}{C}\frac{dC}{dp}\,. \tag{8.1}$$

The lattice must be designed so that over the momentum range, the momentum compaction remains small.

The particle motion in longitudinal phase space depends on its arrival time at the RF cavities, which varies as a function of circumference and velocity v. To first order the time difference with respect to the reference particle is:

$$\frac{\Delta T}{T_0} = \eta\frac{\Delta p}{p_0} = (\alpha_0 - \frac{1}{\gamma^2})\frac{\Delta p}{p_0}, \tag{8.2}$$

where T_0 and α_0 are the revolution period and momentum compaction of the reference particle; ΔT and Δp are the time and momentum deviations, respectively, of the off-momentum particle relative to the synchronous particle with momentum p_0; η is the *phase slip* factor; γ is the Lorentz relativistic factor, and $\alpha_0 = \alpha(p_0)$. The transition energy γ_t is defined by $\alpha = 1/\gamma_t^2$.

In an isochronous ring $\eta = 0$, so to first order the arrival time is independent of the momentum; i.e., $\gamma_t = \gamma$. For 2 TeV muons $\gamma \approx 2 \times 10^4$, so $\alpha \approx 2.5 \times 10^{-9}$. In a regular FODO lattice, α is much larger. To bring the first order value of α to zero requires that the $\langle D/\rho \rangle$ through all of the dipoles be equal to zero, where D is the dispersion and ρ the radius of curvature.

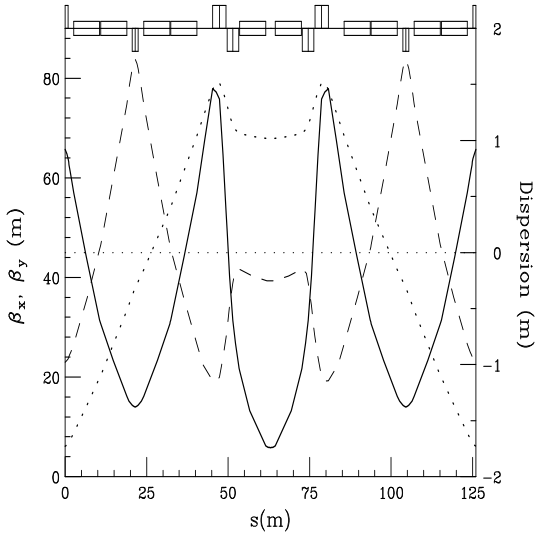

Figure 8.2: Betatron (β_x solid-line; β_y dash-line) and dispersion (dot-line) functions of an arc-module.

In a FODO lattice α is positive. This muon collider ring design has bending regions in the insertions with a FODO structure whose contributions to α are positive, so the contributions of the arcs must be negative with nearly the same magnitude as those of the insertions. For the present design, the value needed for each arc is $\alpha_{\rm arc} = -1.15 \times 10^{-4}$.

This value of $\alpha_{\rm arc}$ can be obtained by building an arc whose periods are FMC modules. An FMC module[4] is a structure composed of two FODO cells separated by a matching insertion which transforms $(\beta_x, \alpha_x, \beta_y, \alpha_y, D, D')$ to $(\beta_x, -\alpha_x, \beta_y, -\alpha_y, D, -D'.)$

The contribution to α of the module can be adjusted by choosing the appropriate value of D with $D' = 0$ at the end of the module. For the module design used here (see Fig.8.2), the matching insertion contains two quadrupole doublets and two dipoles. The two quadrupole gradients and drift lengths are adjusted to bring α_x, α_y and D' to zero at the center of the module. The number of modules and the bending angles of the dipoles are chosen to give the entire arc the bending angle of 152° needed to close the ring.

The arc modules also contain sextupoles; there are two families adjusted to bring the chromaticities of the arc to zero.

Dispersion suppressor A dispersion suppressor module is located at each end of the arc. The purpose of these modules is to bring the dispersion and its slope to zero values in the adjacent insertions.

The suppressor on the downstream end just before an insertion is shown in Fig.8.3; the upstream suppressor is obtained by reflection. This suppressor module is identical to a

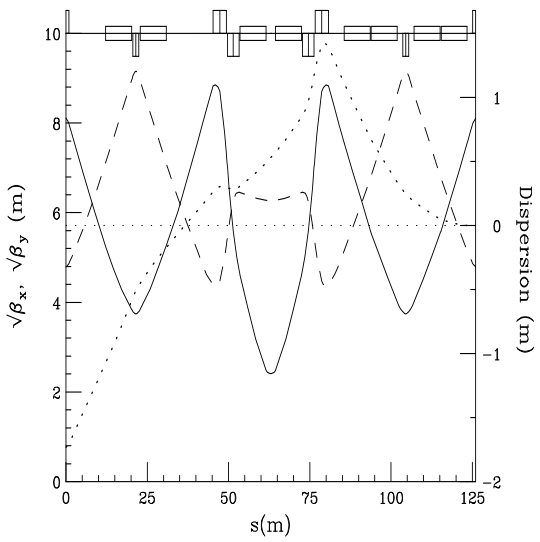

Figure 8.3: Betatron (β_x solid-line; β_y dash-line) and dispersion (dot-line) functions of a dispersion suppressor module.

regular module except that the first four dipoles have been replaced by two dipoles with normal length and different field values. The missing dipoles have been replaced by drift spaces so that the quadrupoles and sextupoles are not changed.

Experimental insertion The design of an insertion with an extremely low-beta interaction region for a muon collider[5] presents a challenge similar to that encountered for the Next Linear Collider (NLC)[6]. The design used here for each half of the symmetric low-beta insertion follows the prescription proposed by Brown[7]; it consists of two telescopes with a chromatic correction section between. Fig.8.4 shows the left half of the insertion, starting at the end of the arc dispersion suppressor and ending at the IP.

The first telescope, called the Matching Telescope (MT), on the left of the figure, brings the beta functions from the arc to a focus of about 3 cm. To the right of the MT lies the Chromatic Correction Section (CCS), which contains two pairs of non-interleaved sextupoles. One pair, situated at positions of maximum β_x and large dispersion D, corrects horizontal chromaticity; the other pair, at maximum β_y positions, corrects vertical chromaticity. The horizontal-correcting pair is farthest from the IP, and the vertical-correcting pair is closest. The sextupoles of each pair are separated by betatron-phase intervals of $\phi = \pi$, and they are located at positions where the phase interval from the IP is an odd multiple of $\pi/2$. To the right of the CCS, the Final Focus Telescope (FFT) transports the beta functions from a focus of a few centimeters to a 3 mm focus at the IP.

The low beta-function values at the IP are obtained with four strong quadrupoles in

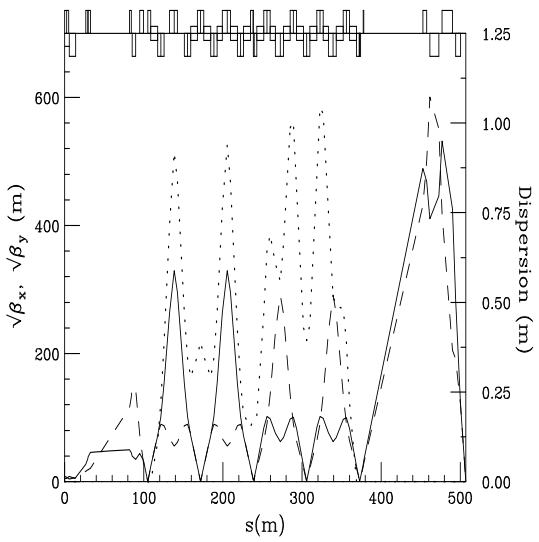

Figure 8.4: Experimental insert (half) with extremely small beta function at the IP.

the FFT with high beta values; these generate large chromaticities, which are corrected locally with the two sextupole pairs in the CCS. This sextupole arrangement cancels the second-order geometric aberrations of the sextupoles, which reduces the second order tune shift by several orders of magnitude. The momentum bandwidth of the system is limited by third-order aberrations and residual second-order amplitude-dependent tune shifts. These aberrations arise from: a) small phase errors between the sextupoles and the final quadruplet; b) finite length of the sextupoles.

The residual chromaticities could be reduced with additional sextupoles at locations with nonzero dispersion, as suggested by Brinkmann[8]. Finally, a system of octupoles could be designed to correct third-order aberrations. Overall, it is believed possible to construct a system with a bandwidth of $\approx 1\,\%$.

The most complex part of the insertion is the CCS. A somewhat oversimplified description follows. The CCS consists of eight FODO cells, each with $\pi/2$ phase advances. The first four cells from the left begin at the center of a QF quadrupole and contain the two horizontal S_x sextupoles, which are next to QFs; the next four cells begin at the center of a QD quadrupole and contain the vertical S_y sextupoles, which are next to QDs. The low-beta focus at the beginning of the CCS repeats itself every two cells and produces the high beta values needed in the sextupoles. The dipoles are placed in a way to cancel the dispersion and its slope at both ends of the CCS and to produce dispersion maxima in the sextupoles.

The strengths of the sextupoles S_x and S_y are adjusted to produce zero first-order chromaticity values for the insertion, while trim quadrupoles are used to minimize the second order chromaticity ($\partial^2 Q/\partial\delta^2$). The complete insertion has very small residual chromaticity,

and is nearly transparent when attached to the arc lattice.

The total length of the half-insertion is 507 m. It contains 44 quadrupoles, 14 dipoles and 4 sextupoles.

Utility insertion The utility insertion closely resembles the experimental insertion, except that the low-beta foci are relaxed in order to lower the beta-function maxima by a factor of about 1000.

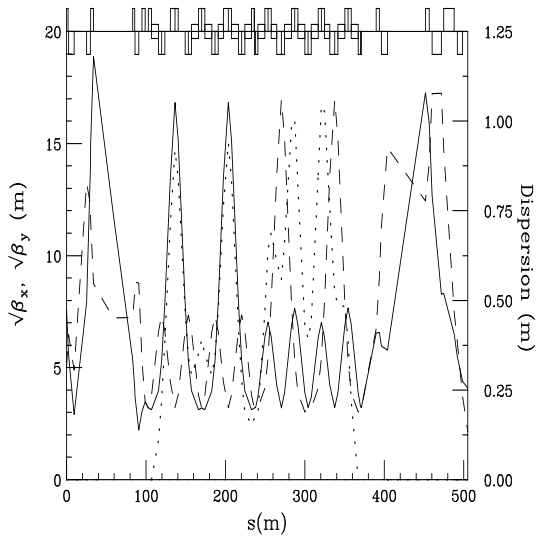

Figure 8.5: Utility insertion (half)

The CCS section for the utility insertion is the same as the one in the experimental insertion, except that the sextupoles are adjusted to cancel the chromaticities of the utility insertion (which are much smaller than those of the experimental insertion). Further changes will probably be needed to accommodate systems for injection, RF, and scraping.

8.2.3 Performance

The variations of the fractional part of the tunes $Q_{x,y}$ as functions of δ are shown in Fig.8.6. Q_y is essentially flat over a bandwidth of $\pm 0.4\%$; Q_x has obvious non-linear components, although the variation of tune, peak to peak is less than 0.04 within a bandwidth of $-0.15\,\%$ to $0.3\,\%$. Likewise, the β^* variation (Fig.8.7) is negligible within a bandwidth of $\pm 0.3\,\%$. The remaining figures show the chromaticity (Fig.8.8), the momentum compaction α (Fig.8.9) and the amplitude dependent tunes $dQ/d\epsilon$ (Fig. 8.10), versus δ. ¿From the results shown in

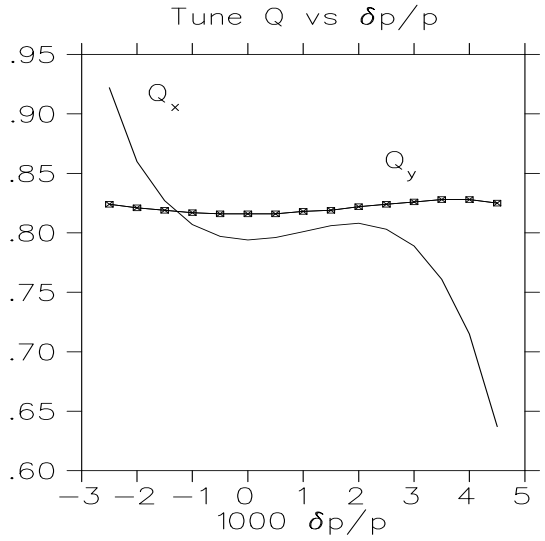

Figure 8.6: Fractional tunes $Q_{x,y}$ vs $\frac{\Delta p}{p}$

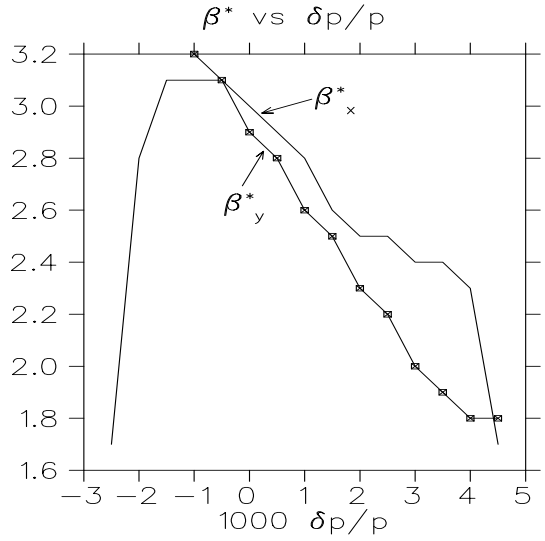

Figure 8.7: Beta function β^* vs $\frac{\Delta p}{p}$

the above figures, it appears that the momentum aperture of the CD has a range $\delta = \Delta p/p$ of 0.007.

The variation of the momentum compaction factor α versus δ, shown in Figure 8.9, is too large to preserve short bunches with a moderate rf voltage. Methods for coping with this problem are discussed in the following section.

Tracking runs [11] using TEAPOT indicate that the dynamic aperture (about one sigma) is too small by roughly a factor of four. The lattice is presently being tuned to increase its dynamic aperture and, along with recent improvements, the aperture has been increased to

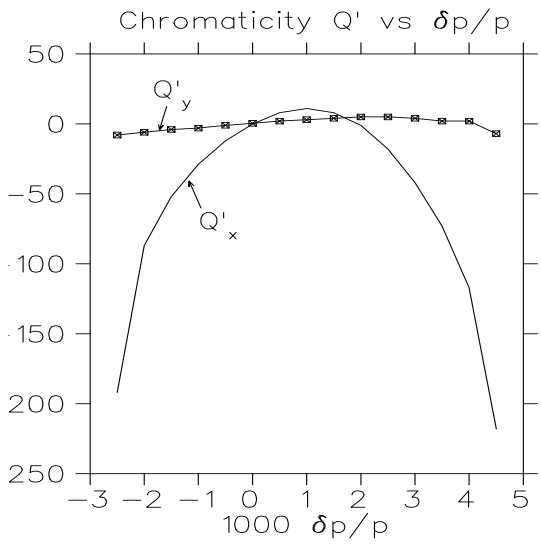

Figure 8.8: Chromaticity vs $\frac{\Delta p}{p}$

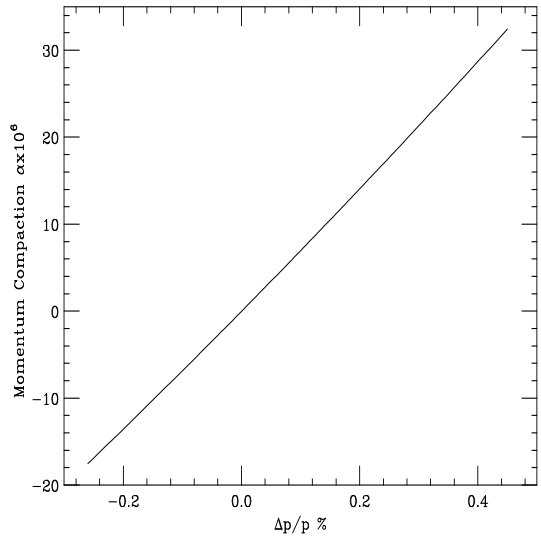

Figure 8.9: Momentum compaction α vs $\frac{\Delta p}{p}$

about five sigma without changing its basic structure. The improvements and adjustments to the collider lattice are outlined in Section 8.2.5.

8.2.4 Control of the Momentum Compaction

The collider ring lattice has been adjusted to be approximately isochronous for the reference particle. That is, the lattice has been designed so that the momentum-compaction factor,

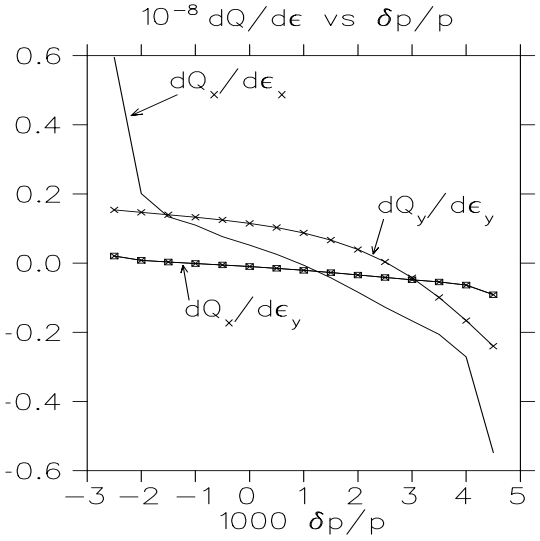

Figure 8.10: Amplitude dependent tune shift $\frac{dQ}{d\epsilon}$ vs $\frac{\Delta p}{p}$

$\alpha(p)$, defined by

$$\alpha(p) = \frac{p}{C}\frac{dC}{dp}\,. \tag{8.3}$$

is approximately zero. In practice, in order to maintain a 3 mm bunch and a modest rf, $\alpha(p_0)$ must be about 10^{-6}.

However, over the desired momentum aperture, $\alpha(p)$ varies, as shown in Figure 8.8, so that over the momentum range of $\pm.004$, $\alpha(p)$ exceeds 10^{-5}. If we expand $\alpha(p)$ in powers of $\delta = p/p_0 - 1$:

$$\alpha(p) = \alpha_1 + \alpha_2\delta + \alpha_3\delta^2 + \mathcal{O}(\delta^3) \tag{8.4}$$

we see from Figure 8.9 that $\alpha_1 = 0$, and $\alpha_2 = 0.006$. This value of α_2 leads to an unacceptable longitudinal head-tail instability. Since α_2 has a contribution from each sextupole of $-2SD^3$, where S is the strength and D is the dispersion in the sextupole, it is possible to correct α_2 with one or more sextupole families.

Initially, horizontal and vertical chromaticities, but not the α_2, of the arcs, experimental insertion and utility insertion were canceled using three independent pairs of sextupole families. Alternatively, the chromaticities of the ring, most of which arise from the experimental insertion, can be canceled by using only the insertion sextupoles. This frees the arc sextupoles to control α_2. Specifically, by inserting a horizontal sextupole next to each of the central F quadrupoles in the arc modules, the α_2 term can be eliminated.

It is possible to control both the linear α_2 and the quadratic α_3 coefficients using two sextupoles pairs in each module, one pair next to the two center QFs and the other pair next to the QF at the module ends–see Figure 8.2. By choosing appropriate strengths for

the different sextupole families, one can make $\alpha_2 \simeq \alpha_3 \simeq 0$, which reduces the variation of α over a range in δ of $\pm.004$ to only about 10^{-7} (for the arcs). Unfortunately, this method halved the total stable momentum range of the ring.

Another way to control α_2 without generating a contribution to α_3 is to pair sextupoles separated by phase intervals of π in the arcs. Thus we conclude that control over both α_2 and α_3 can be achieved to a precision of 10^{-7}; however, this degree of correction may not be necessary (especially for α_3).

In summary, the isochronicity of the ring can be controlled precisely. The momentum-compaction coefficients chosen for the ring will be based on rf bucket and collective instability calculations.

8.2.5 Collider lattice comparisons

As mentioned previously, a different design for the muon collider has been developed by K. Oide[2]. For discussion purposes, the detailed design presented in this document will be referred to as the CD (collaboration design) and Oide's design as the OD. Since tracking results show the OD to have larger dynamic aperture than the CD, the following discussion of the salient differences between the two lattices may be useful.

For the arcs, the CD uses FMC modules, while the OD adopted the KEK B factory modules. Since the dynamic aperture problems arise from the IR, not from the arcs, this difference is probably unimportant.

Both the CD and the OD are similar to linear collider IRs, but there are important differences between these two designs. In the CD the maximum horizontal and vertical beta-function values, and consequently the chromaticities, are equalized. On the other hand, in the OD, the horizontal β_{xmax} is less than β_{ymax} by more than an order of magnitude. As can been seen from the table, the OD ring has a substantially larger vertical high-beta value (900 vs. 350 km) than the CD, and its apertures are correspondingly larger. The vertical chromaticity comparison is less dramatic, since the increased β_{ymax} is offset by the shortened length of the high-beta quadrupoles.

The unequal β_{max} values in the low-beta quadrupoles of the OD compensates for the chromatic correction scheme which favors the vertical plane, due to the fact that the vertical sextupoles are closer to the IP than the horizontal ones. (Increased nonlinearities in the x plane are caused by the intervening y-plane sextupoles.) Thus, for a 2-TeV muon collider, it appears that an asymmetry in chromaticity may be important for chromatic correction.

The strength of the chromatic correction sextupoles is another contributing factor to nonlinearites. In the OD, increased dispersion and much higher β functions allowed the

correction sextupole strengths to be reduced by almost an order of magnitude compared with those of the CD.

The last important feature of the OD to be mentioned here is the addition of octupole and decapole components in the IR quadrupole fields; this addition appeared to increase the dynamic aperture dramatically.

Modifications to the present CD currently under investigation include use of unequal maximum $\beta_{x,y}$ values, optimization of the chromatic correction section, use of higher multipole corrections, and addition of permanent-magnet quadrupoles between the IP and the first superconducting quadrupole.

8.2.6 Summary

Studies have been underway to improve the experimental insertion. The approach of placing permanent magnets within 2 m of the IP to reduce β_{max} and chromaticity has been discarded. Exposure to the high radiation environment in a muon collider ring raised concern over the magnetic field lifetime of a permanent magnet. Instead, a "Bitter" quadrupole is being considered as an alternative magnet to place near the IP. In a preliminary design by B. Weggel during the Snowmass conference, a small "Bitter" quadrupole was introduced with a pole-tip field of just under 4 T. Shielding modifications included placing tungsten collimators between the superconducting IR quadrupoles to shadow and thus protect them from the high backgrounds. To be effective, the collimators had to be 15 cm long with a 4-sigma aperture (the quadrupoles have a 5-sigma aperture). Additionally, sweep dipoles were placed about a meter upstream of the final-focus quadrupoles to eliminate the muon-decay products generated in the preceding long drift. In the previous IR design, most of the decay products struck the IR quadrupoles, creating the unacceptable heat loads.

The combined effect of adding dipoles and collimators to the IR allowed the protective tungsten liner of the superconducting elements to be reduced from 6 cm to 2 cm. This allowed the effective gradient of the final-focus quadrupoles to be increased. When the Bitter quadrupole was also included and placed 4 m away from the IP, peak β functions decreased by almost a factor of two, and chromaticities by a factor of 3 in the horizontal plane and 2 in the vertical. Higher order aberrations were reduced by about two orders of magnitude.

Initially, the dynamic aperture did not increase as a consequence of the IR improvements. The reason for this proved to be the CCS. Optimization work on the CCS proved to be as important as the improvements made to the IR. To maximize momentum aperture, the peak β functions in the chromatic correction sextupoles were deliberately large, which had the

intended effect of reducing their strength and therefore their contribution to higher-order aberrations. However, the large beta functions in the sextupoles increased significantly their contribution to amplitude-dependent tuneshifts. A better way to decrease sextupole strength (and length) is to increase the dispersion function at their locations. Increasing the dispersion and reducing the peak β functions at the sextupoles was the approach used to minimize their higher-order contributions to the amplitude-dependent tuneshifts (without increasing aberrations significantly). When peak β functions in the CCS were reduced from 100 km to 50 km, tracking showed the on-momentum aperture to be 5 sigma. The full momentum acceptance was .3%. Results were found to be strongly tune-dependent and a phase trombone was introduced into the collider ring to adjust tunes independently and without disturbing the lattice. Presently a 10−km version of the CCS with same final focus structure is being tested.

After the FT and CCS optimization is complete using only sextupoles, the addition of octupoles and perhaps decapoles will be studied to further reduce the amplitude-dependent and aberration terms. Also, in future, it is hoped that the "Bitter" quadrupole, which has a high power consumption, can be removed if high T_c superconductor research indicates that we can employ stronger quadrupole gradients in the final focus.

8.3 Superconducting Magnets

The number of collisions during a storage time is inversely proportional to the ring diameter, since the muon decay time constant is fixed by the muon energy. The dipoles in the ring should therefore have a very high field. A reasonable value is 8.5T, supplied by superconducting magnets. As in other rings, the superconductor must be shielded from heat generated by the beam. In the muon collider there are several heat sources: 1) Muon synchrotron radiation, 2) Muon decay (electrons, positron and their synchrotron radiation; neutrinos pass through the walls and do not deposit energy in the accelerator components), 3) Muons that escape from the bunch and hit the vacuum chamber. Estimates show that muon synchrotron radiation is not significant at 2 TeV and that muons that escape from the bunch can be held to a low level. Thus the main contribution to the heating comes from the decay electrons and positrons hitting the inner wall of the vacuum chamber and the synchrotron radiation they emit hitting the outer wall. Secondary radiation from these impacts in turn deposits energy elsewhere in the aperture. The magnet requirements for a muon collider are thus strongly influenced by the decay of the muons. The muons decay into electrons and positrons with around 35% of the muon energy. In the main ring, this amounts to a significant power deposition in the walls. Either a thick absorber will need to surround the

vacuum chamber, increasing the bore of the magnets, or a magnet design that moves the superconducting coils off the midplane (so that absorbing material in the midplane of the ring can be some distance from the coil) needs to be developed.

This section describes design options for dipoles and quadrupoles for the collider ring. It does not include any discussion about superconducting magnets needed in other subsystems of the muon collider nor those that are part of the detector system around the collision point.

8.3.1 Energy Deposition Due to Muon Decay

The collider will be a single separated function ring of superconducting magnets that guides both the negative and the positive muons. The number of muons that decay in a given length L_T can be estimated using the expression

$$N_d = \frac{N_\mu L_T E_0}{\tau_0 E_T c} \tag{8.5}$$

where N_μ is the number of muons transported through a structure per second, N_d is the number of muons that decay in the structure per second, L_T is the length of the structure, E_T is the muon energy, E_0 is the muon rest energy, c is the speed of light, and τ_0 is the muon decay time constant at rest ($\tau_0 = 2.197 \times 10^{-6}$ s). Equation 8.5 is applicable when the transit time for the muon through length L is less than the decay time constant of the muon at energy E_T. The power deposited into the magnet structure from muon decay can be estimated using the expression

$$P \simeq 0.35 N_d E_{ave} \tag{8.6}$$

where N_d is the number of muons that decay per second (See Equation 8.5), and E_{ave} is the average energy of the muon in the structure. The factor 0.35 in Equation 8.6 is the portion of the muon energy that ends up in the decay electrons or positrons. The remainder of the muon energy is transported out of the ring by the decay neutrinos. Table 8.2 presents calculations for muon decay in each of the accelerator components and the collider ring. Included in the Table 8.2 is the number of turns through the component and the total transit length L_T through the structure. Table 8.2 gives an estimate of the decayed muon power that is transferred to electrons and positrons. This is the portion of the decayed muon power that can end up in the superconducting magnet system. The beam flux of muons that enters the accelerator section is assumed to be 3×10^{12} muons per bunch.

The size of the region where the decay electrons, positrons and synchrotron radiation strike the wall of the vacuum chamber is determined primarily by the kinematics of the decay process. For a $3\,\sigma$ vertical beam size of 4 mm, this region is only about 5 or 6

Table 8.2: Muon decay parameters for various parts of a muon collider

Component	Peak Energy (GeV)	Number of Turns	L_T(km)	Total Muon Decay Rate $10^{13}s^{-1}$	Heating Power (kW)	Peak Heat per unit L (Wm^{-1})
Linac	1.0	-NA-	0.12	1.9	0.6	-NA-
First Ring	9.6	9	2.17	1.2	3.6	1.64
Second Ring	79	12	11.3	0.8	19.7	1.75
Third Ring	250	18	29.2	0.4	36.8	1.26
Fourth Ring	2000	18	227	0.6	378	1.66
Collider Ring	2000	1000	7.9	13.1	14600	1840

mm high even at muon energies as low as 20 GeV. As stated earlier, however, secondary interactions cause considerable energy deposition to occur throughout the aperture, so all of the aperture must be considered in the design of any energy-absorbing system. Calculations of energy deposition in the magnet structure are given in section 8.3.4.

8.3.2 Collider Ring Dipoles

The design of the dipoles and quadrupoles is dependent on the percentage of the muon decay product energy that can be removed from within the 4 K mass of the dipole before degradation of magnet performance. Several design approaches can be considered for the superconducting dipole magnets in the collider ring. One approach is to use a conventional cosine theta type of dipole provided the heavy (tungsten) radiation shield is thick enough to reduce the energy into the superconducting coils by about three orders of magnitude. The collider dipole warm bore is about 20 mm. The thickness of tungsten needed to reduce the heating from muon decay by three orders of magnitude is about 65 mm. Thus, the cold bore of the superconducting dipole coils must be 160 mm. The heavy radiation shield could be cooled with a fluid at room temperature. A collider ring dipole with a tungsten liner is illustrated in Fig. 8.11. The energy from the decay products that escapes this liner is well diffused in the coils (see section 8.3.4). Another approach to building collider ring dipole magnets is to have the coils completely separated on the mid plane. The iron return yoke would probably be cold because of the heavy supports needed between the yoke and the coils to restrain the attractive forces between coils. The coils must be separated so that less than 0.1% of the energy from the muon decay products ends up in the superconducting coils or

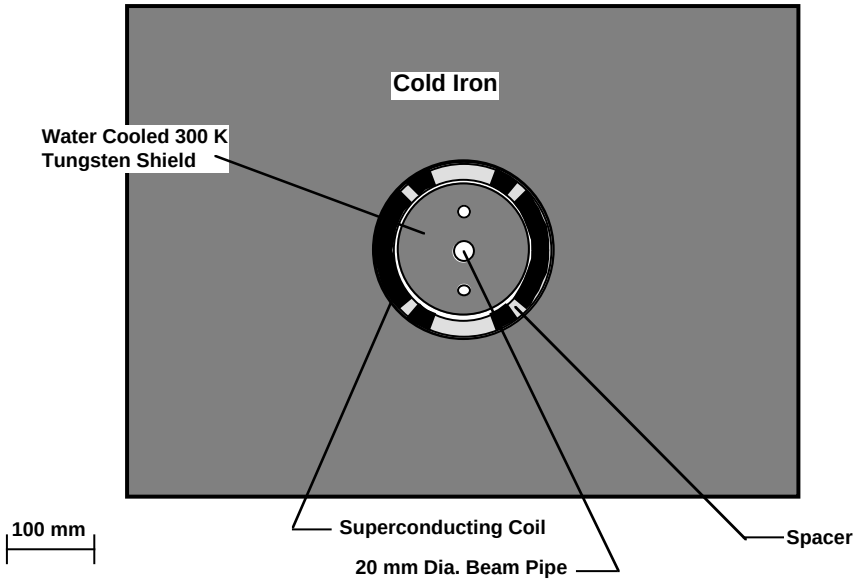

Figure 8.11: A cold iron 8.5 T cosine theta dipole with a 65 mm thick tungsten liner at 300 K

its surrounding support structure that is at 4 K. The rest of the muon decay product energy ends up in the separately-cooled radiation shield. Figure 8.12 shows cold iron dipoles with separation between the coils to allow for a warm vacuum chamber. The dipoles shown in Fig. 8.12 have reasonably good field quality.

Calculations by I. Stumer (private communication) suggest that almost all of the muon decay energy could be captured in absorbers placed at the ends of the magnets. The absorbers would have narrow apertures to capture as much of the radiation as possible yet allow passage of the beam; these narrow apertures may present beam impedance problems. Further work is necessary to confirm the viability of this promising approach.

8.3.3 Collider Ring Quadrupoles and Sextupoles

Several designs can be considered for the collider ring quadrupoles. 1) A design with a thick tungsten liner, similar to the dipole of Fig. 8.11, can be made. With the same 160 mm cold bore aperture, a gradient of 100 T/m could be achieved. 2) A figure-of-eight conventional quadrupole with a pole radius of 12 mm can be used. Conventional quadrupoles of this size can achieve a gradient of 100 to 120 T/m. Most of the muon decay energy can be absorbed by a cooled absorber outside the quadrupole. 3) A quadrupole can be designed that has its coils off the mid plane, Fig. 8.13. This quadrupole design is similar to the dipole design shown in Fig. 8.12. Depending on the field allowed in the superconductor, quadrupole gradients of 140 to 180 T/m can be achieved.

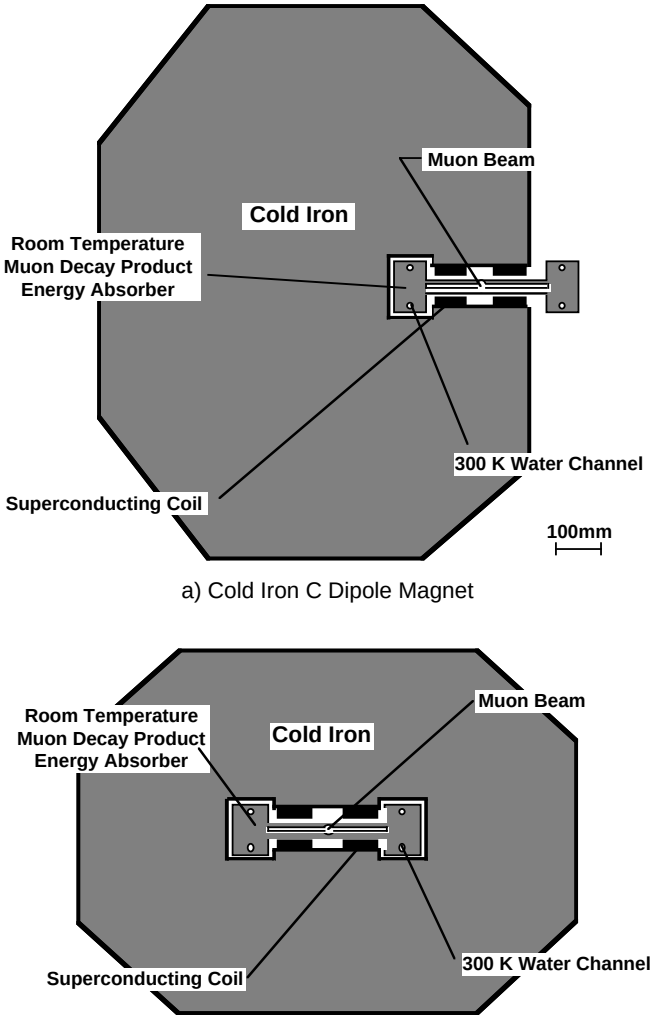

Figure 8.12: Two versions of an 8.5 T cold iron split dipole that would have less than 0.1% of the muon decay power deposited within the superconducting coils

The tuning sextupoles for the collider ring can be conventional. If these sextupoles have the pole at a radius of 12 mm, gradients as high as $3000\mathrm{T/m}^2$ may be achieved. There appear to be no superconducting sextupole designs able to absorb the muon decay products that can achieve this gradient.

8.3.4 Reduction of Heat Load in SC magnets

Due to muon decays, about 2 kW of power are deposited every meter along the collider ring.This results in a heat load that significantly exceeds levels that can be tolerated by existing SC magnets. The energy-deposition distributions in the storage ring components

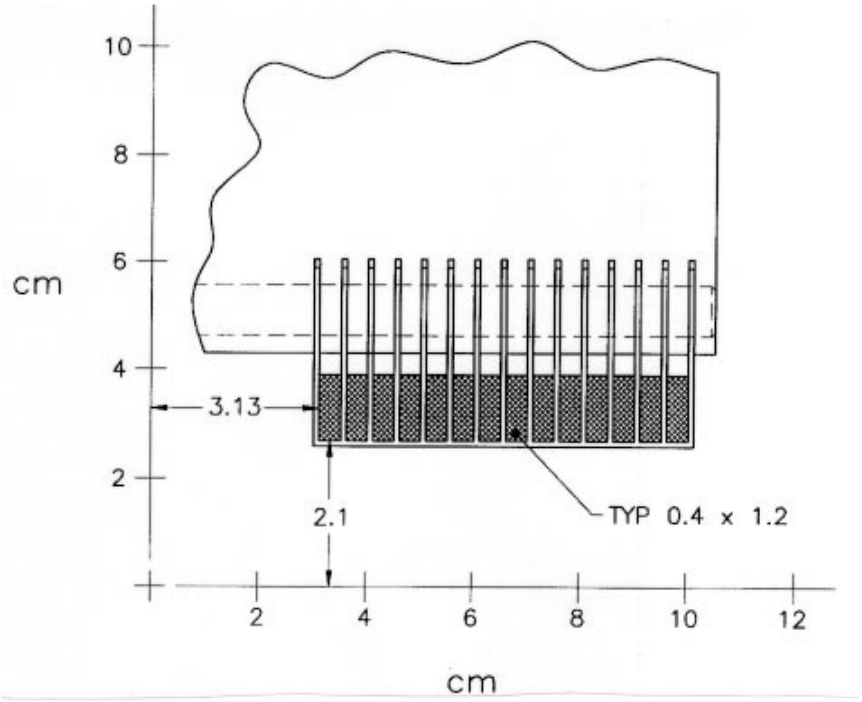

Figure 8.13: A quadrupole design that avoids superconductor on the midplane so that muon decay particles can escape. The drawing shows one pole of the design

from muon decay have been calculated for a 2 TeV muon beam with the MARS code [12]. Even with a longitudinally uniform source, there is an increased background at the high-β_{peak} locations near the IR. Fig. 8.14 shows the azimuthal distribution of power deposited in the first cable shell of the arc SC magnets with tungsten liners of different thicknesses. There is a significant azimuthal dependence of power density due to the effect of the strong magnetic field. The lateral gradient of energy deposited in the SC coil is very strong both with and without a liner. The peak power density exceeds the expected quench limits for the magnet of the assumed type by more than an order of magnitude. A 4 cm tungsten liner provides a considerable reduction of the maximum power deposition density from the quench stability standpoint (see Fig. 8.15). Another concern is the power dissipation in the cold magnet components. As mentioned above, up to 1 kW of power per each beam would be deposited in every meter of the lattice, which is about 1000 times above a possible limit for such extended systems as a collider ring. Fig. 8.16 shows power dissipation in tungsten liner, liquid helium, SC coils, yoke and cryostat components as a function of the liner thickness per one meter of the arc lattice per one beam. One sees that 6 cm liner is required in the arcs in a cosine theta approach. The studies show that in the interaction region two quadrupoles nearest to the interaction point also need at least 6 cm of tungsten shield in front of the SC

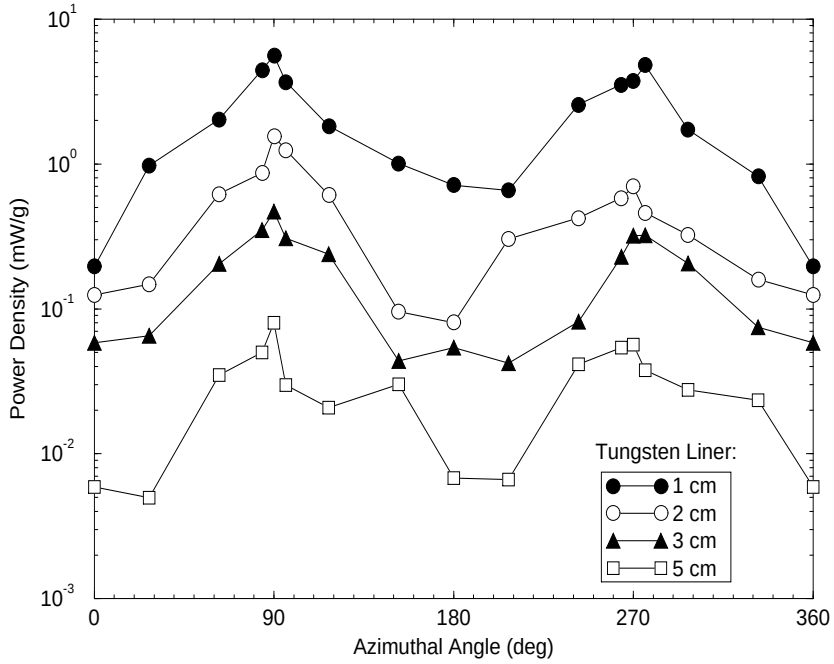

Figure 8.14: Azimuthal distribution of power density in the first SC cable shell in the collider arc for different tungsten liners inside the aperture for 2 TeV muon beam decays

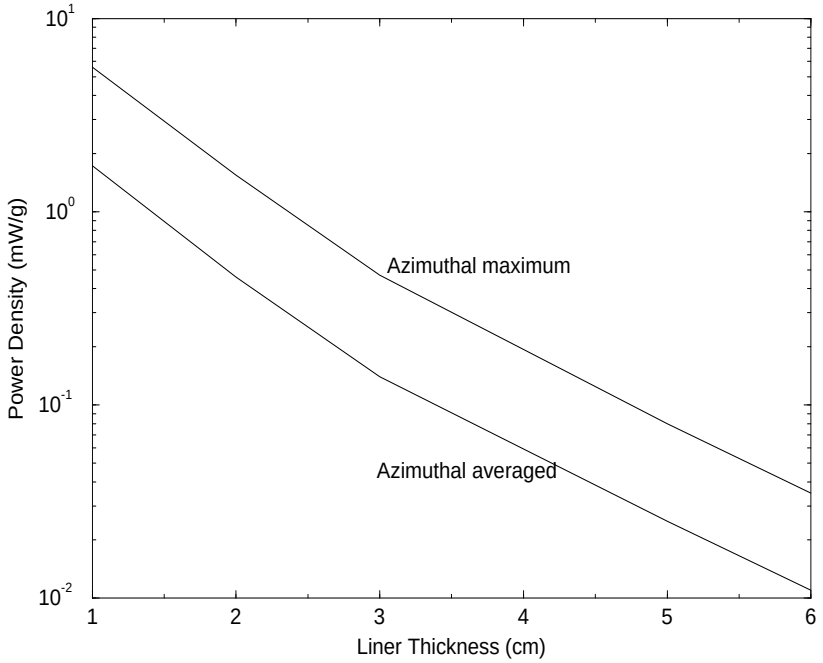

Figure 8.15: Maximum and azimuthal averaged power density in the first SC cable shell in the collider arc *vs* tungsten liner thickness for 2 TeV muon beam decays.

coils in order to reduce the power deposited in the cold mass to the level of ≈ 1 W/m. Even with that, the heat load would be higher compared to that in the arc magnets. This can be tolerated locally, but preferably another solution should be found. A 3 cm tungsten liner is fine for the rest of the IR.

8.4 Radio-Frequency System for the Collider Ring

A radio-frequency system is required for the muon collider ring principally to maintain the tight longitudinal focusing of the muon bunch. It is needed also to make up the energy lost by the beams to higher order mode (HOM) losses in the vacuum system, synchrotron radiation and resistive losses in the walls of the beam pipe.

The beam and collider-ring parameters used in this subsection, which may differ slightly from those in Table 8.1 are in Table 8.3. Two factors influence the choice of rf frequency. The short bunch can be maintained with less voltage at the higher frequencies, while the wakefields and losses are smaller at lower frequencies. The 10-cm wavelength SLAC linac structure was considered as a prototype, but it had to be rejected because of the very large

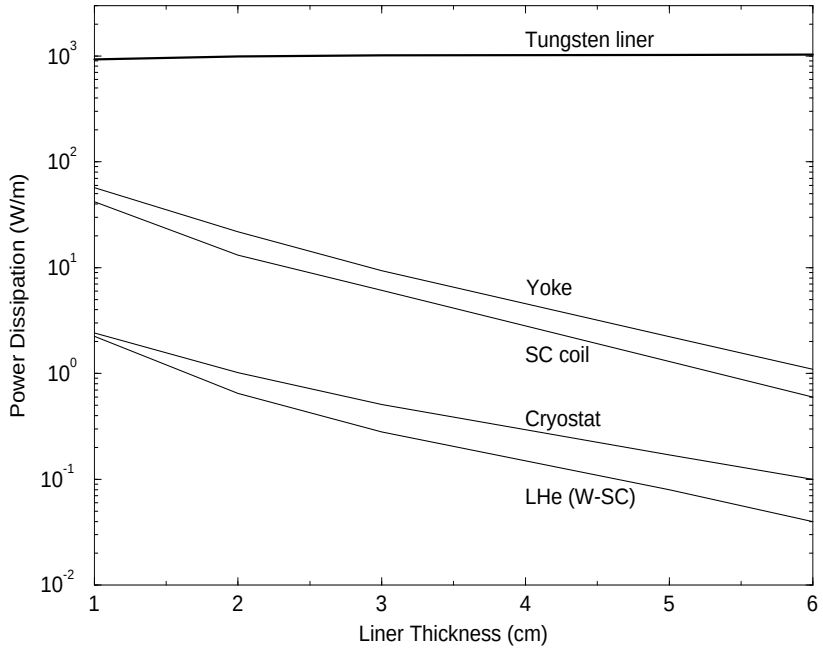

Figure 8.16: Power dissipation in the arc magnet components *vs* tungsten liner thickness for 2 TeV muon beam decays.

distortion of the rf wave shape by the higher order mode losses in the rf cavities by the high-intensity muon bunch. In the SLAC-type structure, in which an average accelerating field strength of 20 MV/m can be utilized, the peak wakefield voltage is estimated to be 15 MV/m, which would cause an intolerable distortion of the rf accelerating field [14].

Table 8.3: Collider parameters used for the rf system

rms bunch length	σ_z	3 mm
rms energy spread	σ_E/E	1.5×10^{-3}
longitudinal emittance	$\epsilon_L = \sigma_E \sigma_z / c$	3×10^{-2}eV-sec
collider circumference	2πR	7 km
revolution frequency	f_0	43.8 kHz
compaction factor	α	10^{-6}
muon storage time		1,000 turns

This led to our considering a TESLA-type rf system–a cryogenic, 1.3 GHz (23 cm wavelength), standing-wave system, which can be operated at 25 MV/m average accelerating field strength and in which the peak wakefield distortion due to the muon bunch is estimated to

be in the range of 3 or 4 MV/m. An rf bucket that is matched to the longitudinal emittance of the muon beam requires 130 MV peak voltage. The corresponding, nominal synchrotron tune ν_s is 5.6×10^{-4} synchrotron oscillations per turn, so that in the 1,000-turn storage time of the muon it undergoes only about 0.56 of a synchrotron oscillation.

Since the loading time of the TESLA structure (800 microseconds) is much longer than the revolution time of the muon beams (23 microseconds), the rf pulse length in the muon collider must extend over the storage time on the muon beam, which is 23 milliseconds or greater. The nominal TESLA operation is with 1.3 millisecond pulses at 10 pps, so that operation with much longer pulse lengths needs to be ascertained.

The dynamics of the muon beam in longitudinal phase space is being investigated with a self-consistent particle-tracking program. We approximate the single-particle wake potential for the TESLA structure, with the SLAC wake potential scaled to the TESLA frequency [15] and adjusted to fit the amplitude of a wakefield voltage distribution as calculated by Mosnier [16] for the TESLA structure. The computer program is self-consistent in that the wake fields are continually recalculated, taking into account the evolving beam shape and distribution in longitudinal phase space.

The wakefield simulation, which includes muon decay, has been used to study the longitudinal dynamics in the ring. The simulations assumed a constant slippage factor of 10^{-6}. The potential well distortion can generate large motion of the bunch center. With a nominal bunch offset of 0.082 radians oscillations of the bunch center, which have a peak amplitude of order .6cm at zero offset, are reduced to less than 0.05 cm.

Even with an offset, the bunch shape evolves during the storage time. The rms bunch length σ_z initially drops from 3 mm to a minimum of about 2.5 mm at about turn number 340 , then rises to a maximum of 3.2 mm at turn 760, and then falls again, reaching about 2.8 mm at turn 1,000. The rms energy spread σ_E/E initially rises from 1.5×10^{-3} to about 2.0×10^{-3} at turn 350, then descends to a minimum of 1.5×10^{-3} at turn 750, and then rises again, reaching about 1.85×10^{-3} at turn 1,000. The longitudinal emittance slowly increases by about 7 percent over the 1,000 turns. These oscillations can be seen in Fig. 8.21 in Sec. 8.8. Further studies exploring methods to reduce the bunch shape oscillations are underway.

The peak wakefield voltage gradient at the first turn was about 4.4 MV/m and the beam-loading factor, defined as the average energy loss per muon divided by the peak rf energy gain is 10%.

The useful bucket area is very sensitive to the slope of the lattice compaction factor with energy. The "design" lattice in Sec. 8.2 envisions an α for which the contributions from nonlinear (in energy deviation) terms is negligible. Nevertheless, it is worthwhile to

determine the limits longitudinal dynamics place on the maximum allowable values of the nonlinear momentum compaction terms (i.e., α_2, and α_3 as discussed in Sec. 8.2).

The bunch has resistive-wall losses [17] of be about 15 MeV/turn/muon in a room-temperature copper beam pipe of radius 1.7 cm and an intensity of 2×10^{12} muons and an rms length of 3 mm. This loss is comparable to the higher order mode losses in the rf cavities, so that the voltage-wave distortion due to these resistive losses must be considered as well. These resistive losses must be replenished by the rf system, but they do not change the parameters significantly as bunch length effects are dominant. Studies of higher order mode losses in the rest of the ring are underway.

8.5 Ring Vacuum Chamber

The choice of ring parameters requires a careful study of beam tube power fluxes and beam tube vacuum issues. These include calculations of the flux, energy and power of particles that escape from the bunches in the collider ring and estimation of where they will hit the walls. Sources of such power at the walls are synchrotron radiation of muons and decay electron-positrons, as well as the decay electrons and positrons themselves and any muons that escape from the bucket. Significant effort will need to be invested in determining, and controlling phenomena that may lead to the escape of particles from the beam core into a halo as well as in the design of a beam halo scraping system which will reduce the flux of lost muons into the detectors and superconducting coils. Some possible mechanisms are the classical beam-beam interaction, hard scattering with background gas or in the beam-beam interaction, incoherent and coherent pair production at the IP, and nonlinear dynamics. The consequences of a muon leaving the bucket need to be carefully studied since a muon that leaves the ring will not be stopped by the shielding, and may deposit energy in the superconducting magnets and create detector background. The current thinking is that only 10^{-6} of the muons can be allowed to escape per turn.

8.5.1 Particle Fluxes

Excluding escaping muons, the three sources of particle flux that strike the beam tube wall are:

- synchrotron radiation from the circulating muons,
- electrons and positrons from the decay of the muons and

- synchrotron radiation emitted by the decay electrons and positrons before they strike the beam tube.

The particle flux, characteristic energy and power flux of each of these is summarized in Table 8.4. For these estimates we have assumed there are two bunches for each muon charge with 2×10^{12} muons per bunch at injection. The intensities and power levels are average values taking account of muon decay and sum the contributions from both signs of muons. The muon energy is assumed to be 2 TeV so the muon lifetime is $\tau_\mu = 41.6$ msec and fresh bunches are injected at 15 Hz, $T_{rep} = 66.7$ msec. At the present time it is undecided whether or not surviving muons will be extracted prior to each injection. For the estimates in Table 8.4 we assume they are not. If surviving muons are extracted just prior to injection of fresh bunches then the intensities and powers are multiplied by the fraction 1 - $exp(-T_{rep}/\tau_\mu) = 0.80$. The bend field is taken to be B = 9 T ($\rho^B = 741$ m) over two thirds of the ring so the total circumference including straight sections is 7.0 km ($T_{rev} = 23.3$ μsec). We have omitted muons diffusing past the dynamic aperture from Table 8.4 since the rate hasn't yet been estimated from tracking calculations. The goal for treating these halo muons would be to intercept as many as possible with a beam scraping and collimation system at a few isolated locations far removed from the detector - e.g. in the utility region on the opposite side of the ring. The particle fluxes in Table 8.4 are distributed uniformly around the ring with synchrotron radiation of course only in the bends. For comparison with the fluxes in Table 8.4 we will give the halo muon numbers that correspond to the provisional 10^{-6} loss probability per turn, all time averaged and without extraction of surviving muons and summed over both signs of muons: 2.14×10^{11} lost $\mu^\pm/s$, 68.5 kW lost $\mu^\pm$ beam power. The particle loss rate is more than three orders of magnitude less than the muon decay rate and the power level is about twice the $\mu^\pm$ synchrotron radiation power. The $\mu^\pm$ however are much more penetrating than $e^\pm$ and photons so they present special problems for shielding the detector and superconductor.

The most important thing to notice in Table 8.4 is that the largest particle flux is synchrotron radiation from muons while the largest power flux on the beam tube is due to $e^\pm$ from muon decay and the associated $e^\pm$ synchrotron radiation. Synchrotron radiation from $\mu^\pm$ is all absorbed on the outside of the ring. The synchrotron radiation loss per turn is 1.05 MeV. The radiation damping time is $\sim 2 \times 10^6$ turns, or a factor $\sim 10^3$ times greater than the muon lifetime. The $e^\pm$ are all absorbed on the inside of the ring and the synchrotron radiation from $e^\pm$ is divided with some falling on the inside and some on the outside of the ring. The amount of energy each $e^\pm$ radiates before it hits the beam tube and the fractions of $e^\pm$ synchrotron radiation absorbed on the inside and outside of the ring depend on the

Table 8.4: Time average $\mu^{\pm}$ particle fluxes, characteristic energies and power incident on the beam tube assuming no extraction of surviving muons prior to each injection. All rates are summed over both signs of muons.

Source	Intensity	Characteristic energy	Power
	particles/m/sec		W/m
$\mu^{\pm}$ syn. rad.	5.7×10^{16}	$E_c = 2.7$ keV	7.7
$e^{\pm}$ from $\mu^{\pm}$. decay	1.7×10^{10}	$< E > = 700$ GeV	1500
			(=1900-400)
$e^{\pm}$ syn. rad.	2.3×10^{12}	$< E_c > = 2.1$ GeV	400

detailed geometry and dimensions of the beam tube. So far two general situations have been discussed: (1) a warm cylindrical beam tube surrounded by an absorber with $cos(\theta)$ coils at cryogenic temperatures on the outside and (2) a warm beam tube with a slot on the inside radius to allow $e^{\pm}$ to escape and strike an absorber which is placed outside the cryogenic windings of C - magnet coils. In the second case an additional smaller absorber at the outside radius would be inside the C-coils and absorb synchrotron radiation. For estimates in this preliminary report we will assume a simple warm cylindrical beam tube with radius $r_w = 1.0$ cm. In that case $\mu^{\pm}$ synchrotron radiation photons travel a sagittal distance 3.85 m before striking the outside radius of the beam tube at an angle 5.2 mrad. Looking at the particle energies in Table 8.4, the $\mu^{\pm}$ synchrotron radiation is relatively soft with critical energy 2.7 keV. These photons will be absorbed on the surface of the beam tube and photodesorb a significant amount of gas estimated in Sec. 8.5.3 below. Photodesorbtion by $\mu^{\pm}$ synchrotron radiation will determine the gas pressure in the beam tube, thermal desorption is relatively unimportant even for an unbaked beam tube. The $e^{\pm}$ and accompanying synchrotron radiation are enormously more energetic than the $\mu^{\pm}$ synchrotron radiation and will produce electromagnetic showers that penetrate deeply into the shielding and magnet structure surrounding the beam tube. The $e^{\pm}$ have a broad energy spectrum that extends from essentially zero to the full 2 TeV $\mu^{\pm}$ energy. The mean $e^{\pm}$ energy is equal to $0.35 \times E_{\mu} = 700$ GeV. The $e^{\pm}$ synchrotron radiation parameters given in Table 8.4 have been averaged over the $e^{\pm}$ energy spectrum. The $e^{\pm}$ synchrotron radiation in the 9 T bend field is large enough that its effect in reducing the $e^{\pm}$ energy before intercepting the beam tube must be taken into account or the magnitude of synchrotron radiation will be overestimated. For example in a 9 T bend field the mean critical energy averaged over the $e^{\pm}$ spectrum from 2 TeV muon decay is 4.2 GeV; this is reduced to 2.1 GeV when account is taken of synchrotron radiation reducing the $e^{\pm}$ energy and the average is taken over the path length from the

point of emission to the point of intercept with the beam tube at $r_w = 1.0\,\text{cm}$. Similarly the power radiated by $e^{\pm}$ has been integrated over the $e^{\pm}$ spectrum and corrected for emission of synchrotron radiation. The $e^{\pm}$ radiate about 20% of their energy before striking the inside radius of the $r_w = 1\,\text{cm}$ beam tube. This radiation energy has been subtracted from the decay energy received by $e^{\pm}$ in Table 8.4 to avoid double counting the energy reaching the beam tube. Absorbing the $e^{\pm}$ and accompanying synchrotron radiation and shielding the superconducting cable and detectors will be serious design challenges. These last two particle fluxes however should not have a significant impact on the beam tube vacuum.

8.5.2 Beam Gas Scattering and Beam Tube Gas Density Requirement

Circulating muons undergo two types of collisions with gas molecules in the beam tube that can cause deleterious effects: (1) multiple small angle Coulomb collisions and (2) single large angle nuclear Coulomb collisions. In the absence of significant radiation damping multiple small angle collisions cause a steady increase in beam emittance and loss of luminosity. Setting the emittance growth time equal to 10^4 turns, approximately ten times the luminosity lifetime, sets an upper bound on average beam tube gas pressure of 3.1 mTorr CO scattering equivalent. Single large angle nuclear Coulomb collisions can lead to a betatron amplitude that exceeds the dynamic aperture of the collider ring or intercepts a physical aperture. Here we assume the dynamic aperture exceeds the physical aperture. The characteristic physical apertures in the collider ring are summarized in Table 8.5. The IR quads have the smallest aperture with $H/\sigma = 3.1$ normalized to the beam rms beam size in one transverse dimension. In reality there will be a halo scraper yet to be designed with normalized aperture somewhat smaller then the IR quadrupoles. For estimating single large angle scattering loss we will assume a limiting aperture $H/\sigma = 3.1$. A loss probability of 10^{-6} per turn has been provisionally adopted as a limit for beam halo losses that can be tolerated by the detectors. Allowing a large angle scattering loss probability of this same magnitude leads to a beam tube gas pressure requirement of less than 4.2 mTorr CO scattering equivalent, not too different than the multiple scattering requirement. Because of the relatively short storage times in a muon collider and different collision characteristics compared to electrons and protons, the beam tube vacuum requirement is enormously more relaxed than in conventional electron and proton storage rings. This is a fortunate and perhaps even necessary circumstance since dealing with the large particle and power fluxes of $e^{\pm}$ from muon decay may restrict the possibilities for pumping.

Table 8.5: Characteristic apertures and rms beam dimensions in the collider ring. Note that $\epsilon = \sigma^2/\beta = 2.65 \times 10^{-9} m - rad$

Location	Lattice β (m)	σ (mm)	aperture radius H (cm)	H/σ
Arc	50	0.28	1.0	35.7
IP	3×10^{-3}	2.2×10^{-3}	.025	114
IR quad	360,000	24.0	7.5	3.1

8.5.3 Sources of Beam Tube Gas and Estimate of Beam Tube Gas Density

The two most significant sources of gas molecules in the collider beam tube are:

- photodesorbtion by $\mu^{\pm}$ synchrotron radiation and
- thermal desorption.

To estimate the beam tube pressure due to photodesorbtion we use experimental measurements of $E_c = 3$ keV photodesorbtion coefficients on a LEP aluminum vacuum chamber [18]. Photodesorbtion coefficients decrease steadily with photon exposure as molecules in the surface oxide layer are desorbed and pumped out. For our numerical estimates we take the magnitudes of desorption coefficients after exposure to 10^{21} photons/m. This corresponds to a few hours of operation of the muon collider ring at design intensity, a modest conditioning time. Similarly the outgassing rate of unbaked vacuum chambers decreases steadily with time and to be specific we take outgassing rates characteristic of chemically cleaned aluminum after 100 hours of pumping [19]. Accurately calculating the pressure from the gas sources depends on the detailed dimensions of the beam vacuum chamber and location and sizes of vacuum pumps. Here we are only interested in an order of magnitude estimate so we take what is probably a worst case - a beam tube with radius $r_w = 1.0$ cm and pumped only at 20 m intervals, a reasonable allowance for the length of superconducting dipole magnets. We also assume the beam tube is near room temperature owing to the requirements of removing the large power fluxes due to muon decay. In this situation it is trivial to choose vacuum pumps so the effective pumping speed is limited by and essentially equal to the conductance of the beam tube. With these assumptions the gas loads and beam tube axially averaged partial pressures in Table 8.6 have been calculated. The beam tube pressure is effectively dominated by the photodesorbtion of CO and CO_2 and taken together amount to about 10^{-4} Torr CO scattering equivalent, more than an order of magnitude below the requirement discussed in the previous section. The partial pressure of the dominant gas due

Table 8.6: Estimated sources of gas and average partial pressures in the collider beam tube.

gas	Q/photo	$\langle p \rangle$	Q/thermal	$\langle p \rangle$
	Torr cm^2 sec^{-1}	Torr	Torr cm^2 sec^{-1}	Torr
H_2	2×10^{-5}	2×10^{-5}	4×10^{-8}	3.6×10^{-8}
CH_4	3×10^{-7}	8×10^{-7}	3×10^{-9}	8×10^{-9}
H_2O	-	-	2×10^{-6}	5.4×10^{-6}
CO	10^{-5}	3.4×10^{-5}	3×10^{-8}	1×10^{-7}
CO_2	10^{-5}	4.3×10^{-5}	3×10^{-9}	1.3×10^{-8}

Table 8.7: Resistive wall dissipation for Cu, Al and SS beam tubes.

material	$\langle p \rangle$(MW)	$\langle p/L \rangle$(W/m)	$\langle \Delta W \rangle$(MeV/turn)
Cu	.59	83.6	17.1
Al	.74	106	21.5
SS	3.8	543	111

to thermal outgassing - H_2O is approximately 20 times less than the sum of photodesorbed CO and CO_2. Eventually, as photodesorbtion cleans up the CO and CO_2, thermal outgassing of H_2O may become the dominant beam tube gas component during operation.

8.5.4 Beam Tube Resistivity and Image Current Losses

The image current of the bunched muons will be carried on the surface of the beam tube in a thin layer with thickness of the order of a skin depth. This current will drive an Ohmic loss that is estimated in Table 8.7 for copper, aluminum and stainless steel, assuming a beam tube with radius $r_w = 1.0$ cm, two bunches for each sign of muon with 2×10^{12} muons per bunch injected, no extraction of surviving muons prior to each injection and an rms bunch length $\sigma_z = 3$ mm. The results in Table 8.7 are time averaged, taking account of muon decay. The average muon energy loss per turn in Table 8.7 is an intensity weighted average. For copper and aluminum the resistive wall energy loss exceeds the synchrotron radiation loss by a factor of approximately twenty.

8.6 Classical Beam-Beam Interaction

A preliminary look at the classical beam-beam interaction for the muon collider has been carried out [20]. The rest of this Section is taken from Ref. [20]. The beam-beam simulations

for the muon collider in the incoherent classical approximation, taking into account muon decay, show that for the nominal intensity of 2×10^{12} per bunch the beam-beam interaction is reasonably weak and allows room for upgrading the luminosity performance. The analysis shows that classical coherent beam-beam effects will almost certainly not spoil the beam luminosity lifetime. The beam-beam effects become noticeable if the number of particles is increased by a factor of three or more. These conclusions are based on the assumption that the dynamical aperture is sufficiently large (say, 5σ or larger). For a smaller aperture nonlinear lattice dynamics will need to be included in the calculation.

8.6.1 Introduction.

The classical beam-beam effects arise from the interaction of the particles in one beam with the classical electromagnetic fields of the opposing beam. The fundamental dynamics is the electromagnetic deflection of the particles. Quantum beam-beam effects deal with particle annihilation and creation as described by relativistic quantum mechanics.

Incoherent effects are those that are well described by the interaction of a single particle in one beam with the other beam (or by the simple superposition of such interactions), while coherent effects are those that can only be explained by the interaction of the beams with each other as whole.

A basic example of an incoherent classical effect is the blowup of the beam core (emittance blowup) as the beams collide turn after turn; as a consequence of this blowup the luminosity degrades, at least to some extent. In this case the phase space of the core particles remains essentially structureless (approximately gaussian in the case of e^+e^- machines). Another example is the development of large-amplitude tails in the particle distribution, which leads to a decrease of the beam lifetime as the particles are gradually lost to the machine aperture. In this case, the phase space of these large amplitude particles has a characteristic structure that is dominated by one or more resonances arising from the combined dynamics of the beam-beam force and the nonlinear magnetic fields of the machine. These two phenomena dominate the beam-beam dynamics of essentially all hadron and lepton colliders built so far. For well-tuned e^+e^- colliders with good dynamic aperture, these effects have vastly different time scales: the core blowup always happens over a few damping times, while the development of significant tails can be arranged to happen over thousands of damping times or even longer [21].

The signature for classical coherent effects is a nontrivial structure of the phase-space of the core particles. This space structure can arise when the tune is close to a low-order resonance. An example of this kind of effect is the flip-flop state in e^+e^- colliders: in this

case, for sufficiently high bunch current, the two beams reach an equilibrium situation in which one of them is blown up while the other is not. This effect has been observed in most colliders. Other coherent states that have been predicted in simulations, and perhaps observed experimentally, are period-2 or -higher fixed points, in which the sizes of the two beams fluctuate from turn to turn in a periodic pattern. Simulations generally show that the time scale for these effects is of the order of 10-20 damping times [22, 23].

An example of an incoherent quantum effect for the muon collider is the reaction $\mu^+ + \mu^- \to e^+ + e^-$ that can happen during the beam-beam collision. A muon can also interact with the collective electromagnetic field of the opposing bunch to produce e^+e^- pairs; this is a coherent quantum effect. The latter effect is believed to be negligible for this ring, while the former is addressed in Sec. 8.7.

In this section, however, we will show that incoherent classical effects are weak, at least for nominal parameter values, and that coherent classical effects are very unlikely to materialize. We will also provide rough criteria for the tolerances for the ratio β^*/σ_z, and for the longitudinal displacement of off-IP collisions which can arise from RF phasing errors or from timing errors in the injection process.

8.6.2 Physics of the Incoherent Simulation.

We carry out a simulation with the code TRS [24]. This is a "strong-strong" simulation in which both beams are dynamical, and their emittances evolve according to their mutual interaction. The simulation is fully six-dimensional, and the beam-beam interaction is represented as a thick lens by dividing up the bunches into 5 "slices." We assume one bunch per beam, and a single interaction point (IP). The beams are represented by "macroparticles" (1024 per bunch in this case), and the machine lattice is assumed to be strictly linear, so that it is represented by a simple phase advance matrix. This linear approximation is valid provided that the dynamical aperture is sufficiently large (say, 5σ or larger). The three tunes are taken as input quantities to the simulation, and we set the chromaticity to 0. From other work, we know that the values we have chosen for the number of slices and macroparticles are adequate for the nominal muon collider specifications [25].

The beams are described at time $t = 0$ by six-dimensional gaussian distributions whose σ's are determined by the specified nominal parameters of the collider (see Table 8.8). We then let the bunches collide for 1000 turns, keeping track of the six-dimensional coordinates of all the macroparticles, and measure from these the beam sizes and the luminosity at every turn as they evolve according to the beam-beam dynamics. The code uses the so-called "soft-gaussian approximation" by virtue of which, for the purposes of computing the beam-

beam kick, the opposing bunch is *assumed* to have a gaussian shape in the two transverse dimensions, albeit with time-dependent σ's. This approximation is generally reliable provided no coherent effects appear, which is almost certainly the case for the muon collider, as we shall discuss below. We take into account the muon decay by simply multiplying the number of particles per bunch N in each beam by the exponential decay factor $\exp(-t/\tau)$, where τ is the Lorentz-dilated muon decay constant.

8.6.3 Beam-beam Simulation.

Simulation Conditions.

For the purposes of this simulation, we assume parameters as listed on Table 8.8 (both beams have the same parameters). In this table β^* is the common value of the horizontal

Table 8.8: Muon collider parameters.

C [km]	7
E [TeV]	2
N	2×10^{12}
β^* [mm]	3
ϵ_N [mm–mrad]	50
f_c [kHz]	42.86
ν_x	0.57
ν_y	0.64
ν_s	1/160
σ_z [mm]	3

and vertical beta-functions and the same is true for the normalized emittance ϵ_N. The values for the horizontal and vertical fractional tunes ν_x and ν_y were picked arbitrarily (the integral part of the tune does not enter the simulation).

With these values, the beam size at the IP is

$$\sigma^* = \sqrt{\beta^* \epsilon_N / \gamma} = 2.74 \ \mu\text{m} \tag{8.7}$$

where $\gamma \approx 18,900$ is the usual relativistic factor. The nominal value for the peak luminosity is

$$\mathcal{L} = \frac{f_c N^2}{4\pi\sigma^{*2}} = 1.82 \times 10^{35} \ \text{cm}^{-2} \ \text{s}^{-1} \tag{8.8}$$

which is not exactly the time averaged luminosity $\times 10^{35}$ cm^{-2} s^{-1}, as listed elsewhere in these report.

It is worthwhile to note that the beam-beam parameter,

$$\xi = \frac{r_0 N}{4\pi\epsilon_N} = 0.046 \tag{8.9}$$

has a fairly typical value: In fact, beam-beam parameter values like this have been attained or exceeded in several e^+e^- colliders (here r_0 is the classical radius of the muon). Actually, it is intriguing that the values of γ and ξ are similar to those in the former PEP collider, so certain aspects of the incoherent beam-beam interaction can be expected to be similar to those in PEP.

An important parameter in colliding rings is the damping time. Assuming that the synchrotron energy loss per turn in the muon collider is 1 MeV, the transverse damping time is

$$\tau_x = \frac{2 \text{ TeV}}{1 \text{ MeV}} = 2 \times 10^6 \text{ turns} \tag{8.10}$$

which is much larger than the 1000 turns' duration of a cycle. The large difference between these time scales is crucial in explaining some beam-beam effects.

Simulation Results.

Fig. 8.17 shows the luminosity as a function of turn number obtained under the assumption that the muon is a stable particle. One can see that it decreases by $\sim 4\%$ during the course of the 1000 turns due to the incoherent emittance blowup. This fractional decrease is small because the beam-beam parameter is modest, and because the cycle time is so small relative to the damping time.

Fig. 8.18 shows the luminosity taking into account the finite muon lifetime. As expected from the previous result, the curve is essentially determined by the exponential decay factor of the muons.

Fig. 8.19 shows the luminosity *vs.* turn number for three values of the number of particles per bunch N. For each value of N we carried out the simulation for three random number seeds; thus the spread in the curves for each case gives an idea of the statistical errors of the calculation. The bottom curves, corresponding to the nominal value of 2×10^{12}, are the same as in Fig. 8.18. The middle curves, for $N = 4 \times 10^{12}$, still behave quite nominally. However, it is clear that the curves for $N = 6 \times 10^{12}$ decay faster than exponentially due to substantial emittance blowup. In addition, when we included a 10σ physical aperture in the simulation, we observed that there were no particle losses for the first two cases, but there was a $\sim 2\%$ integrated beam loss for the case where $N = 6 \times 10^{12}$. Although this is a small

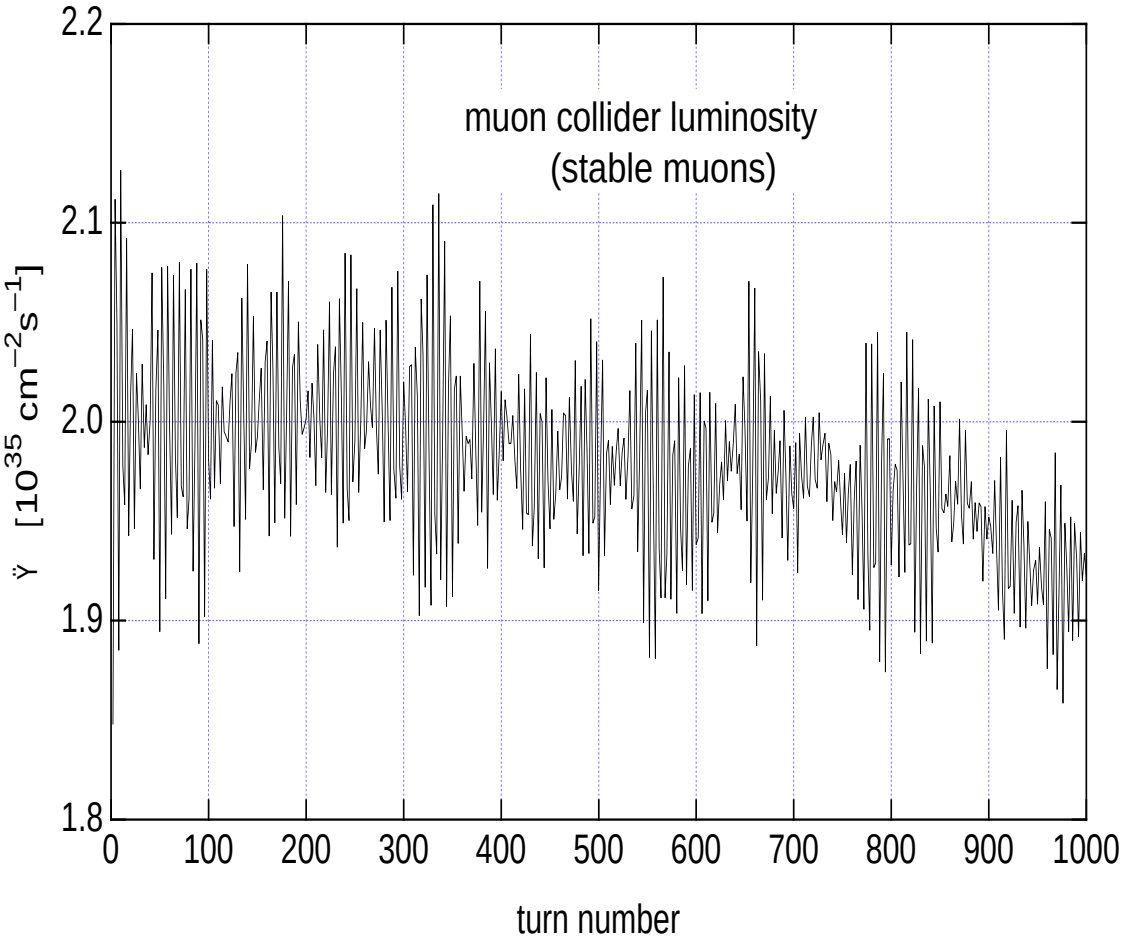

Figure 8.17: Luminosity as a function of turn number assuming that the muons are stable particles. The luminosity decreases by $\sim 4\%$ over 1000 turns due to incoherent emittance blowup.

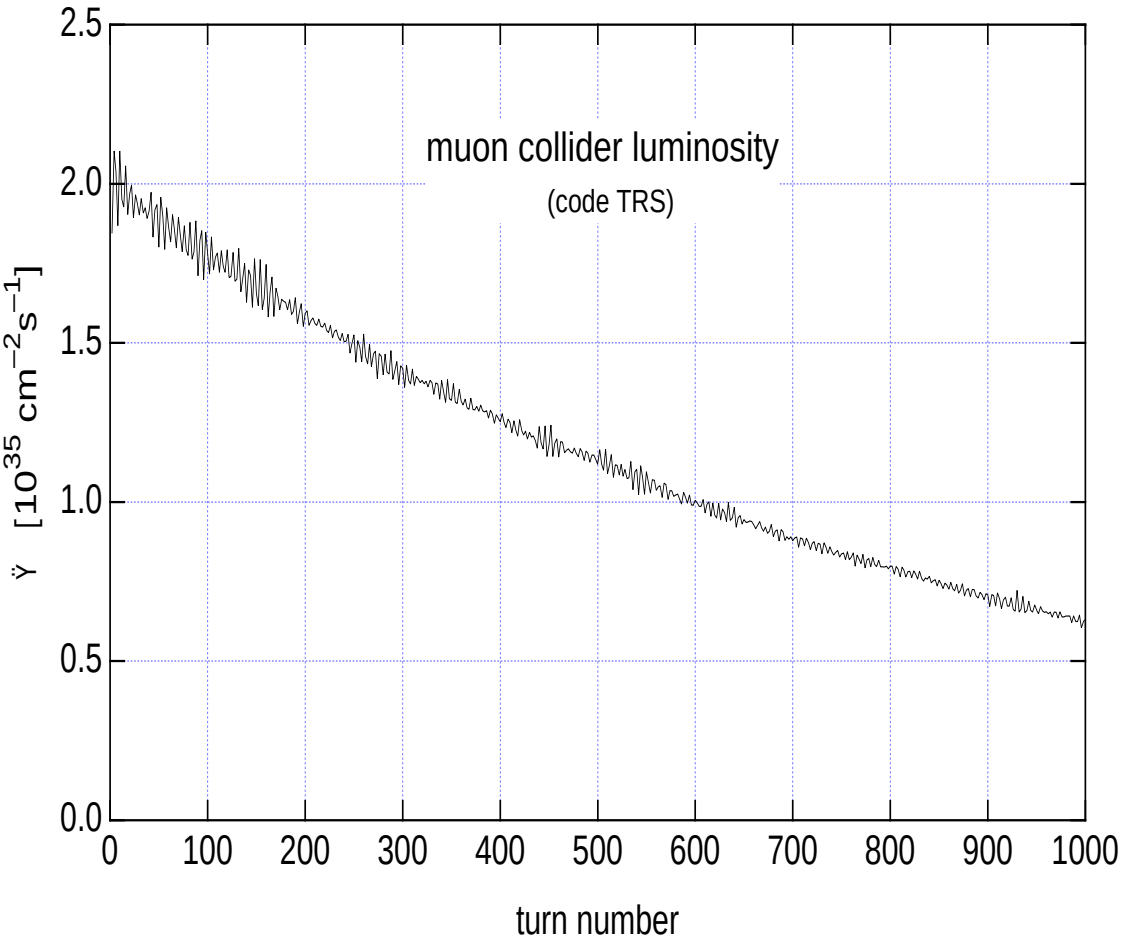

Figure 8.18: Luminosity as a function of turn number, taking into account the finite muon lifetime. The curve follows closely the expected exponential decay dependence.

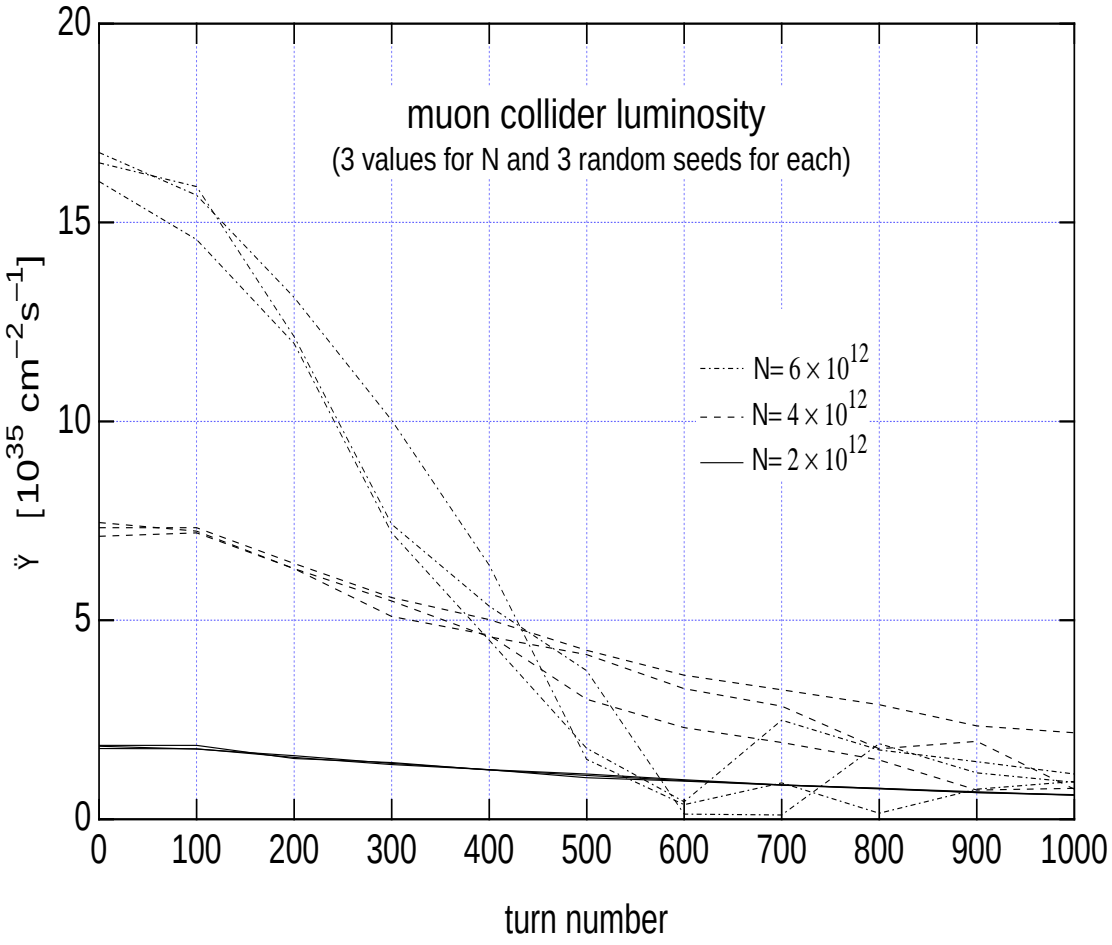

Figure 8.19: Luminosity as a function of turn number for three different values of the number of particles per bunch N. For each case we show three runs, each corresponding to a different random number seed; the spread of the curves for each case gives an idea of the statistical accuracy of the calculation.

fraction of particles, it is reasonable to interpret this as a symptom that the beam-beam strength is being pushed beyond a prudent limit, and the results of this simulation cannot be taken as a reliable guide. When this kind of behavior is seen, it is likely that other detrimental effects, not included in this simulation, will become important and will lead to even more unfavorable behavior. We conclude from this calculation that the incoherent beam-beam effect is weak for the nominal current and that there is some room for upgrading the luminosity by increasing the bunch current by a factor of ~ 2 but not more than this.

8.6.4 Other Classical Beam-Beam Issues.

Coherent Effects.

Classical coherent effects significantly distort the phase space of the beam core away from the gaussian shape. This distortion may be static or time dependent, and leads to luminosity degradation; thus, despite the theoretical interest of these effects, in practice one wants to identify the conditions under which they appear in order to avoid them.

Simulation studies for e^+e^- machines [22] show that these effects materialize for beam-beam parameter values $\gtrsim 0.05$ and for isolated values of the fractional tune where certain low-order resonances dominate the dynamics. More importantly, these results also show that coherent effects take a long time to develop, on the order of 10 damping times or more, simply because it takes a long time for the particles to redistribute in phase space in order to give rise to a clear structure. At the beginning of the simulation (the time scale being set by the damping time), there is no hint of structure, and the phase space distribution is essentially gaussian. This is the situation relevant to the muon collider, since the cycle time is a tiny fraction of the damping time. Furthermore, these results are obtained in the zero-bunch-length approximation, and there are indications [26] that a nonzero bunch length strongly suppresses coherent effects. Although more research is needed, and experimental work under controlled conditions needs to be carried out to confirm the simulation results, we can safely conclude from presently available information that these effects are unlikely to appear in the muon collider.

Beam Tails and Beam-Beam Lifetime.

While the beam core determines the luminosity of a collider, the beam tails determine the beam lifetime. The beam core, typically understood to be the phase space region within $\sim 3\sigma$ of the center, is not very sensitive to nonlinear machine resonances because the lattice magnetic fields are typically quite linear in this region. On the other hand, the beam tail

extends out to sufficiently large amplitudes so that its dynamics is sensitive to an interplay [27] of beam-beam and lattice nonlinearities (beam-gas scattering can also come into play in subtle ways, although typically it has a clearer effect on the beam core).

There has been much recent progress in understanding and properly simulating the beam tails in e^+e^- colliders. These new tools make use of a clever algorithm by which the brute-force tracking is "accelerated" by 2-3 orders of magnitude in order to determine the particle density and flux at large amplitudes (up to $\sim 20\sigma$ or so) [28, 29]. From the particle flux one can then determine the lifetime, given the physical aperture. For the purposes of this article, one can roughly summarize the conclusions as follows: for a lattice with larger dynamic aperture (meaning 5σ or more), and for reasonable values of the beam-beam parameter (meaning 0.05 or less), it is not difficult to find working points for which the beam-beam lifetime is of the order of $10^7 - 10^9$ turns (however, the lifetime can degrade by several orders of magnitude by relatively small changes in these parameters). In any case, the instability of the muon will almost certainly dominate the beam lifetime, so at least from this perspective, the beam tails will not be important.

Thus the beam tails might be much more important for other reasons such as background and radiation. The important thing, therefore, is to specify the maximum acceptable number of muons that can hit the vacuum chamber during the 1000 turns of a cycle. Such a criterion is closely related to that of the dynamic aperture. In the above-mentioned e^+e^- simulations, the damping time, typically of order $10^3 - 10^4$ turns, also plays an important role. The muon collider, as mentioned earlier, essentially has no damping, so in this respect it is akin to proton colliders. It seems therefore that the tracking tools used to determine the dynamic aperture of such machines are the right ones for this case, provided they are augmented to include a beam-beam element. Such a code development should be relatively simple, although the analysis will likely involve many iterations.

Hourglass Effect for Centered Collisions.

Because of the geometrical divergence of the beams at the IP, the luminosity is actually smaller than the nominal value given by Eq. (8.8), which represents the limiting value as the bunch length $\sigma_z \to 0$. As σ_z grows at fixed β^*, the luminosity decreases due to this "hourglass effect." Neglecting all dynamical effects, this purely geometrical reduction factor is given, for symmetric round gaussian beams, by the formula [30]

$$\frac{\mathcal{L}(\sigma_z)}{\mathcal{L}(0)} = \int_{-\infty}^{\infty} \frac{dt}{\sqrt{\pi}} \frac{e^{-t^2}}{1 + (t/t_x)^2} = \sqrt{\pi}\, t_x\, e^{t_x^2}\, \mathrm{erfc}(t_x) \tag{8.11}$$

where $t_x \equiv \beta^*/\sigma_z$. For the muon collider, t_x has been chosen to be unity; β^*/σ_z] It can be shown that the luminosity degrades quickly as σ_z increases.

Hourglass Effect for Longitudinally-Displaced Collisions.

By virtue of the hourglass effect, the luminosity also degrades if the bunches collide at a point away from the optical IP. If the central collision is longitudinally displaced by a distance s_c from the IP (but the bunches still collide transversely head-on), the luminosity reduction factor is given by [30]

$$\frac{\mathcal{L}(s_c,\sigma_z)}{\mathcal{L}(0,0)} = \int_{-\infty}^{\infty} \frac{dt}{\sqrt{\pi}} \frac{e^{-(t-t_z)^2}}{1+(t/t_x)^2} \tag{8.12}$$

where $t_z \equiv s_c/\sigma_z$ and t_x is the same as above. In Fig. 8.20 we show the luminosity reduction

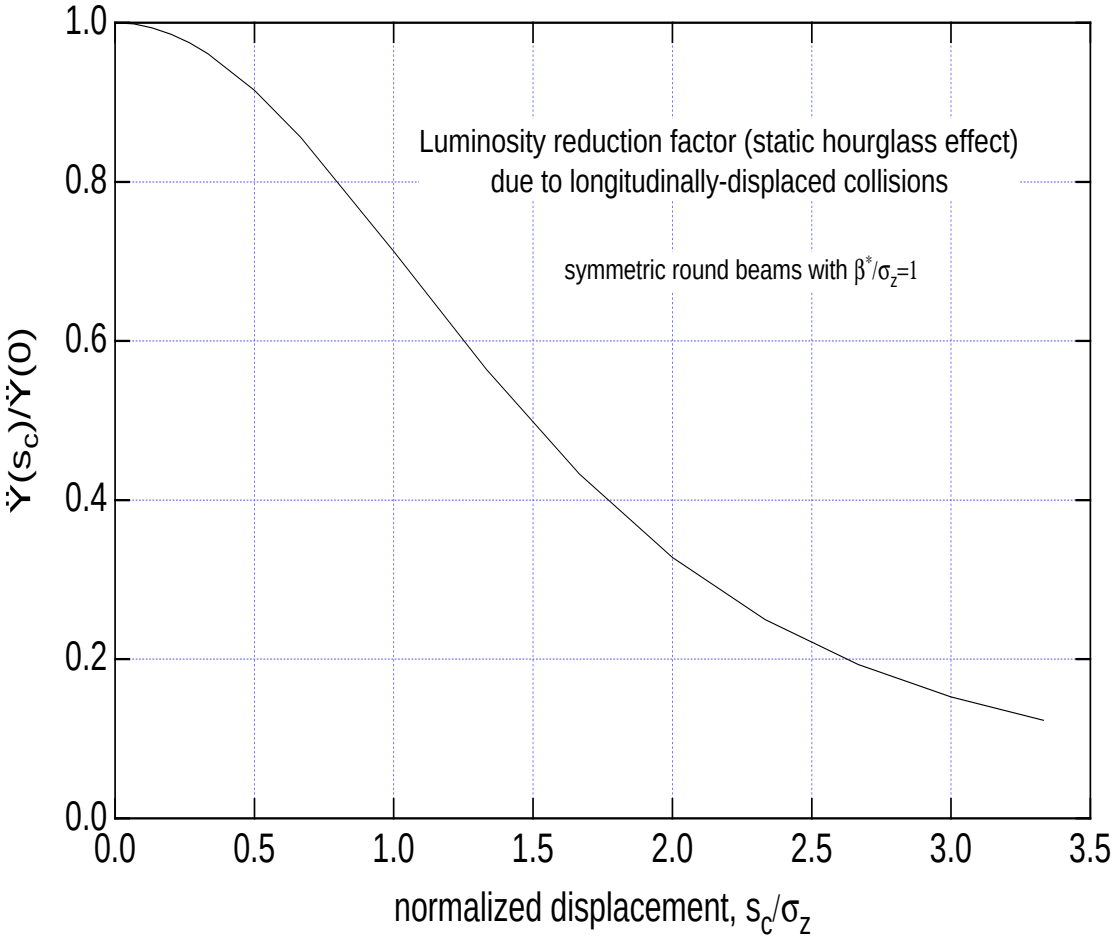

Figure 8.20: The hourglass luminosity reduction factor when the collisions are longitudinally displaced from the IP by a distance s_c, plotted as a function of s_c/σ_z. Note that the normalization is $\mathcal{L}(s_c = 0, \sigma_z = 3$ mm), *i.e.* the nominal value.

factor as a function of t_z (please note that in this figure we have normalized the reduction factor to $\mathcal{L}(0, \sigma_z)$ and *not* to $\mathcal{L}(0, 0)$ as in Eq. (8.12)). One can see that the luminosity degrades quickly when the collision point is farther away than $\sim 1\sigma_z$ from the optical IP. This gives an idea of the RF phasing errors or injection timing errors that can be tolerated.

8.6.5 Summary

We have carried out some basic beam-beam simulations for the muon collider in the incoherent classical approximation, taking into account the muon decay. We conclude that the beam-beam interaction is reasonably weak and allows room for upgrading the luminosity performance. We have argued that classical coherent beam-beam effects will almost certainly not materialize, and neither will long tails that might spoil the beam lifetime. We have provided some very basic constraints on the ratio β^*/σ_z and on off-center collisions arising from the hourglass effect. Finally, we will attempt to prioritize work that remains to be done.

From the perspective of the classical beam-beam dynamics, the four key features that distinguish the muon collider are:

1. A relatively modest beam-beam parameter, $\xi = 0.046$.

2. A short cycle of 1000 turns.

3. A long damping time, $\tau_x = 2 \times 10^6$ turns.

4. Unstable muons.

The first feature is shared with many e^+e^- colliders; the second makes this collider not too different from single-pass colliders; the third one makes it resemble a hadron collider; and the fourth, of course, is unique to this machine. It is fair to say that one can understand all features of the classical beam-beam interaction from the interplay of these four characteristics.

We have shown by means of beam-beam simulations that the classical incoherent beam-beam effect is quite weak for the muon collider in its present design. From this perspective, there is room for upgrading the luminosity, if necessary, by increasing the bunch current by a factor of 2 or so but not more than this.

We have argued that coherent classical beam-beam effects are very unlikely to materialize.

We have also argued that beam tails are unlikely to affect the luminosity lifetime. Undoubtedly there will be a certain number of large-amplitude muons that will hit the chamber,

and it seems important to establish this number. This issue is closely related to the determination of the dynamic aperture, and single-particle tracking tools used for hadron colliders, duly augmented to include the beam-beam interaction, seem appropriate to address this issue.

From purely geometrical considerations, we have provided a rough estimate (probably a lower bound) of the sensitivity of the luminosity to the ratio β^*/σ_z and to the longitudinal displacement of the collision point from the IP. These estimates yield fairly standard results: one should not choose the ratio β^*/σ_z below ~ 1 or so, and one should not allow collisions to be displaced from the optical IP by more than $\sim 1\sigma_z$ in either direction.

Much work remains to be done to firm up the limits imposed by the beam-beam interaction. Here is a brief suggested list, roughly in order of priority:

1. Develop a dynamic aperture tool by augmenting a single-particle tracking code to include a "beam-beam lens."

2. Track specific lattices, including all nonlinearities, and estimate from the results the number of muons that hit the vacuum chamber during 1000 turns; iterate this process to determine tolerances on machine nonlinearities.

3. Establish the sensitivity of the beam-beam interaction to longitudinal and transverse alignment errors and jitter.

8.7 QED Effects at the Interaction Region

A significant source of e^+e^- pairs in the $\mu^+\mu^-$ collider is the *incoherent* process $\mu^+\mu^- \to \mu^+\mu^-e^+e^-$ which has a cross section about 10 mb (at a muon energy 2 TeV). An analysis of the energy distribution of the pairs shows that they may generate a significant and undesirable background in the detector. The bulk of this Section is taken from [32]. The detector design chapter addresses this in further detail.

Coherent pair production in the muon collider occurs as an individual muon interacts with the magnetic field of the opposing bunch at the IP. It is now believed to be an insignificant effect in the parameter regime of the collider. [32].

Since the heat deposition in the collider creates a limit on the number of muons that can hit the wall each turn, we must investigate the energy spectrum of those muons that create pairs, and follow their trajectories. This must be done for muons that pair produce at the IP and for those that decay naturally during the ≈ 1000 turn storage. The characteristic

magnetic field of bunch at the collision point is, for the parameters of Table 8.1,

$$B \sim \frac{eN}{2\sigma_x\sigma_z} \sim 0.5 \times 10^3\ T. \tag{8.13}$$

The asymptotic cross section for the production of e^+e^- pairs at the collision of charged particles was first obtained 60 years ago [33]. A precise treatment of this process, along with numerous references, are can be found in Ref. [34].

A detailed analysis of the main features of the pair production process $pp \to ppe^+e^-$, with numerical estimates, has been considered in detail [35]. This process is similar to the pair production in the muon ring. The equations in Ref. [35] are valid for the muon collider ring, with the evident changes in notation, and some numerical estimates should be reconsidered due to a much higher Lorentz factor in the muon collider.

Some rough estimates of the process are:

1) The total cross section of the process is [36]:

$$\sigma \approx 10\ mb. \tag{8.14}$$

2) The main mechanism for pair creation is the two–photon production of e^+e^- pairs via the collision of two virtual photons which are emitted by the muons. The main features of process can be obtained with the equivalent photon (Weizsäcker–Williams) approximation (EPA). The spectra of virtual photons are found from an analysis of Feynman diagrams. Their dependence on the energy ω and virtuality Q^2 has the form

$$dn(\omega, Q^2) = \frac{\alpha}{\pi}\frac{dx}{x}\frac{dQ^2}{Q^2}\left[1 - x + \frac{x^2}{2} - (1-x)\frac{Q^2_{min}}{Q^2}\right]; \tag{8.15}$$

$$Q^2 \geq Q^2_{min} = m_\mu^2\frac{x^2}{1-x}. \tag{8.16}$$

where $x = \omega/E$ and the last inequality is obtained easily from kinematics.

The cross section for the subprocess $\gamma\gamma \to e^+e^-$ has a maximum when $W^2 \approx 8m_e^2$, where W is the effective mass of the produced system. Therefore, the effective mass of the produced e^+e^- system is near threshold, and the transverse momenta of produced particles is $\sim m_e$. Furthermore, this cross section decreases quickly with the growth of the virtuality Q^2 above m_e^2. In other words, the main contribution to the cross section is in the region

$$m_e^2 > Q^2 > Q^2_{min}.$$

Now, with Eq. (8.16), we obtain the limit for the energy of the photons:

$$x = \frac{\omega}{E} < \frac{m_e}{m_\mu} \Rightarrow \omega < \gamma m_e. \tag{8.17}$$

Therefore, — in accordance with the *naive* expectations — the Lorentz–factor of the produced e^+e^- pair cannot be higher than that of the initial muon.

An integration of Eq. (8.15) over virtuality gives the number of equivalent photons that are produced:

$$dn(\omega) = \frac{2\alpha}{\pi}\frac{dx}{x}\left[\ln\left(\frac{m_e}{m_\mu x}\right) - \frac{1}{2}\right]. \tag{8.18}$$

Note, that this quantity is much lower than that for the two-photon production of muons or hadrons, which is

$$\sim (2\alpha/\pi)(dx/x)\ln(1/x). \tag{8.19}$$

The source of this difference is the much higher upper limit of effective virtualities for these processes, which determined by the much higher scale of the Q^2 dependence for these subprocess. (For more detail discussion see Ref. [34].)

3) The produced pairs are distributed uniformly in the rapidity scale. The distribution over the total energy of pair ϵ is

$$d\sigma = \begin{cases} \frac{56\alpha^4}{9\pi m_e^2}\frac{dk_z}{\epsilon}\left[\ln^2\gamma - \ln^2\frac{\epsilon}{m_e}\right] & \text{at} \quad \epsilon < \gamma m_e; \\ \sim \frac{\alpha^4}{m_e^2}\frac{d\epsilon}{\epsilon}\left(\frac{\gamma m_e}{\epsilon}\right)^2 & \text{at} \quad \epsilon > \gamma m_e. \end{cases} \tag{8.20}$$

Here k_z is the longitudinal momentum of the pair, $|k_z| \approx \epsilon$.

The mean energy of a pair is $\sim 2m_e\gamma/\ln\gamma \sim 2$ GeV. In accordance with Eq. (8.14), the number of pairs produced is about 10^5 per bunch collision, i.e. about 10^8 during the luminosity lifetime in the ring. Therefore, the entire energy losses due to the discussed process are about $2 \times 10^{-6}\%$ of the muon energy, i.e. negligible.

4) The distribution over the energy of one electron ϵ_1, emitted along the motion of initial μ^+, has the form

$$d\sigma = \frac{56\alpha^4}{9\pi m_e^2}\frac{dk_{1z}}{\epsilon_1}\left[\ln^2\gamma - \ln^2\frac{\epsilon_1}{m_e}\right] \quad (\epsilon_1 \gg m_e). \tag{8.21}$$

Here k_{1z} is the longitudinal momentum of the electron. The effective mass of produced pairs is near the threshold and their total transverse momentum is very low. Therefore, the bulk of the electrons and positrons move initially in the same direction as the beam.

However, as was pointed out by Palmer [37], the created electrons are deflected by the magnetic field of the opposing muon bunch and may fly into the detector. Detailed studies of this potentially serious problem are being carried out by the detector group.

8.8 Single Bunch Collective Effects

Introduction

The design of a high luminosity ($2.5 \times 10^{30}\text{cm}^{-2}$ per collision) muon collider ring, from the perspective of the physics of collective effects, has some unique features which need to be examined. (1) Muons have a very short life time: $\tau_\mu \simeq 41.6$ ms at 2 TeV, corresponding to a thousand "effective" turns in a ring with the circumference of 7 kilometers. (2) The bunch is short: $\sigma_z = 3$ mm. (3) The bunch has a large charge: $N = 2 \times 10^{12}$. (4) The momentum compaction α is very small: $\alpha \leq 10^{-6}$. These features lead us to some unusual aspects of the ring operation: The intense bunch required for the high luminosity makes instabilities likely and very small α requires careful estimations of nonlinear corrections to the particle orbit and to the collective dynamics.

The longitudinal equations motion of a particle in a circular machine are

$$z' = -\eta\delta, \tag{8.22}$$

$$\delta' = K(z), \tag{8.23}$$

where z is the oscillation amplitude with respect to the bunch center, $' = d/ds$, s measures distance around the ring, $\delta = dp/p$, $\eta = \alpha - 1/\gamma^2$, $\alpha = pdC/Cdp$. The force $K(z)$ that a particle experiences can be modeled as having two parts, one is due to the radio frequency (rf) cavities, and the other is from the wake fields generated by the interaction between beam and cavities or other components of its electromagnetic environment,

$$K(z) = K_{rf}(z) + K_{wake}(z), \tag{8.24}$$

where

$$K_{rf}(z) = \frac{eV_{rf}(z)}{CE}, \tag{8.25}$$

and

$$\begin{aligned} K_{wake}(z) &= \frac{F_{\parallel wake}(z)}{E} \\ &= -\frac{r_0}{\gamma C}\int_z^\infty dz'\rho(z')W_0'(z-z'). \end{aligned} \tag{8.26}$$

In Eq. 8.26, $T_0 = 2\pi/\omega_0 = C/c$, $E = \gamma m_\mu c^2$, $r_0 = e^2/m_\mu c^2$, $N = \int dz'\rho(z')$, and $C = 2\pi R$ is the circumference of the collider ring.

In Eq. 8.25, when the amplitude of synchrotron motion is small compared with the rf wavelength such that the rf voltage is linearized as $V_{rf}(z) = \hat{V}\sin(\omega_{rf}z/c) \approx \hat{V}\omega_{rf}z/c$ and

the momentum compaction is expanded as $\eta = \eta_1 + \eta_2\delta + \eta_3\delta^2$ (with the contributions from η_2 and η_3 negligible), the synchrotron oscillation frequency is $\omega_{s0} = \left(e\eta_1\, c\,\omega_{rf}\hat{V}/CE\right)^{1/2}$.

The transverse equation of motion is

$$y''(z,s) + \frac{\omega_\beta^2}{c^2}y(z,s) = -\frac{Nr_0}{\gamma C}\int_z^\infty dz'\rho(z')W_1(z-z')y(z',s). \tag{8.27}$$

A simulation code that solves these equations has been developed to study collective phenomena in the ring.

Static Effects

As a starting point we consider a TESLA-like rf system, and a quasi-isochronous lattice which has $\eta_1 = 10^{-6}$, with the contributions from η_2 and η_3 negligible. With a bunch length $\sigma_z = 3$ mm, $\sigma_\delta = 1.5 \times 10^{-3}$ rms energy spread and an 130MV of L-band rf, the muon bunch is matched to the rf and a muon would undergo $\sim .56$ synchrotron oscillations in one thousand turns. The beam-loading factor, defined as $\triangle\mathcal{E}$/particle/V_{rf}, is 10% when only the cavity losses are included. Resistive losses are estimated to roughly equal the rf losses, but have not been explicitly included in our calculation. Other losses have not been calculated, and may lead to an increase in the rf voltage. These loses will need to be replenished even if the momentum compaction is reduced to $\eta_1 = 10^{-7}$, as may be required because of microwave instabilities.

Parasitic Loss The beam loses energy when it experiences the impedance of the rf cavities. The rf impedance is modeled by using Wilson's scaling formula for the longitudinal wake function [15]. Explicitly, choosing as starting point TESLA's rf structure, we use

$$W_0'(z<0) = 226(\frac{f_{TESLA}}{f_{SLAC}})^2 \times \exp[-(|z|\frac{f_{TESLA}}{0.1839 f_{SLAC}})^{0.605}], \tag{8.28}$$

where $f_{TESLA} = 1.3$GHz and $f_{SLAC} = 2.856$GHz. Causality requires: $W_0'(z) = 0$ for $z > 0$. The simulation code computes the wake voltage $V_{wake}(z) = \int_z^\infty dz'\rho(z')W_0'(z-z')$, and the energy loss

$\triangle\mathcal{E} = -\int_{-\infty}^\infty dz\rho(z)\int_{-\infty}^\infty dz'\rho(z')W_0'(z-z')$.

The peak wake voltage is further scaled from Wilson's formula to give parasitic cavity losses 17V/pC/m at $1\sigma_z$ for a Gaussian beam. This choice of wake amplitude makes it consistent with the TESLA rf cavity studies[16].

The effects of radiation and diffusion of muons are small in a muon lifetime (radiation damping time $\sim 10^6$ turns), so that, unlike in electron rings, equilibrium is not achieved by radiation damping. The intense muon bunch generates significant wakes, and these wakes

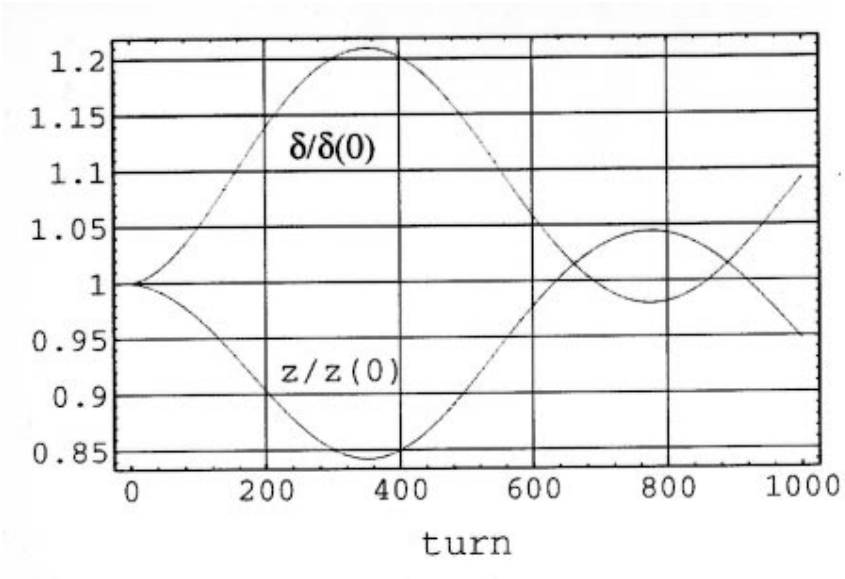

Figure 8.21: Scaled rms bunch size and rms energy-spread vs. turn, where at injection: $z(0) = 3\text{mm}$, $\delta(0) = 0.15\%$.

in turn cause significant changes in the vacuum rf potential. This potential-well distortion causes oscillation of the bunch center, bunch size, and distribution function in the rf bucket. Fig. (8.21) shows the oscillations of the rms bunch size and bunch energy spread. The bunch centroid tends to move forward to a higher rf voltage, so that the energy loss can be compensated. As a result, it makes a counter-clockwise rotation in $\delta - z$ phase space, as shown in Fig. (8.22). The parasitic losses from the rf and motion of the bunch centroid are compensated for by injecting the beam with an rf phase offset of 0.082 radians with respect to the bunch center, as shown by the dashed line in Fig. (8.22).

Coherent Effects

Microwave Instability The microwave instability is presently considered the most serious challenge to maintaining a short bunch. Presently studies are underway to examine the limits this instability places upon Z/n. The ring parameters obviously will not satisfy the Keil-Schnell criterion for stability, but rather hope to reduce the growth rate to an acceptable amount during the ~ 1000 turns of beam storage. The microwave instability growth rate is weaker at smaller η values, and the instability may require the lattice to operate at $\eta = 10^{-7}$. At this value of η the particles barely move longitudinally, and the possibility and consequences of compensating for the wake potential with rf are being considered. In the absence of longitudinal motion the main problem is to maintain an energy spread within the longitudinal acceptance of the ring.

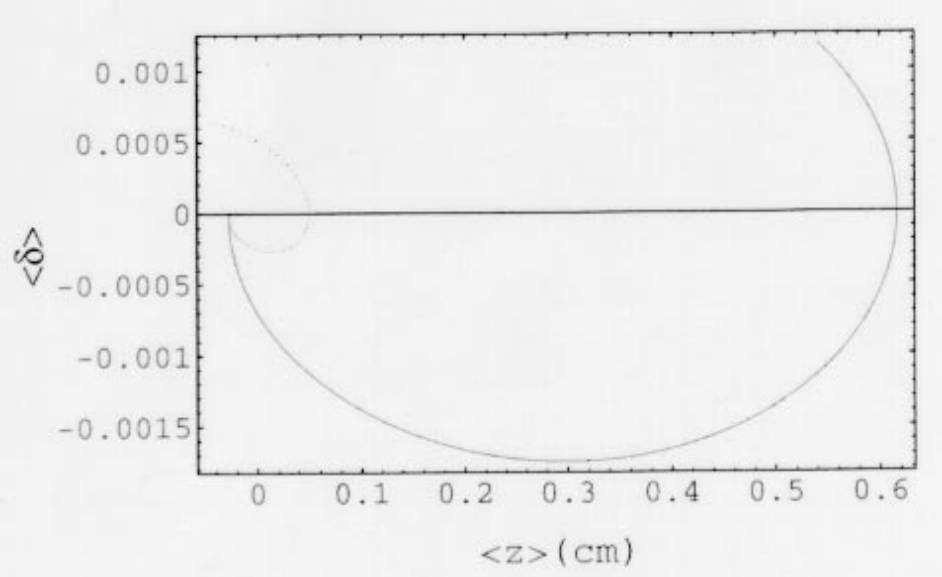

Figure 8.22: Center of energy-spread vs. center of bunch size. The rf phase offsets are, $\phi = 0, 0.082$ radian, for the solid line and dashed line, respectively.

Beam-Break-Up For times much shorter than the synchrotron oscillation period, particles are almost frozen longitudinally in the bunch, and the transverse wakefield dynamics has many similarities with that in a linac [10, 40]. In a linac, the transverse wake field generated by the head of the bunch drives the tail, causing Beam-Break-Up (BBU). A dimensionless parameter that characterizes the BBU strength is [17]

$$\Upsilon(z) = Nr_0|\langle W_1(z)\rangle|c/4\omega_\beta\gamma, \tag{8.29}$$

where ω_β is the betatron angular frequency, and $\langle W_1(z)\rangle = \int_z^\infty dz' W_1(z-z')\rho(z')$ is the convoluted total transverse wake function. The tail of an off-axis bunch doubles its offset in a number of turns $n \simeq 1/\Upsilon$, so long as $n \ll 1/2\nu_s$, i.e., when the particle's synchrotron motion can be ignored.Here ν_s is the synchrotron tune.

Simulation results for the BBU-like instability using a resonator model are shown in Fig. (8.23). The main point is that while the motion is unstable, it is easily cured with only a small amount of BNS damping, as discussed below.

Head-Tail Instabilities When the transverse oscillation frequency is modulated by the energy oscillation, the chromaticity, which is the slope of the frequency to the energy, builds up a head-tail phase that bootstrap from the first half synchrotron period to the next, and drives the system into instability without threshold. This head-tail instabilities occurs in both transverse and longitudinal motion [41]. The effect of transverse head-tail (THT) instability is small when $\eta_1 \leq 10^{-6}$.

For the longitudinal motion, the longitudinal chromaticity involves the non-linear part of slip factor: η_2. The bucket height and the growth time of the longitudinal head-tail (LHT) instability are both proportional to η_1/η_2. Different design of the lattice lead to very different results for the geometry of bucket and the collective effects. It is assumed here that the contributions of η_2 and η_3 to the dynamics are sufficiently small, even if $\eta_1 = 10^{-7}$, that they can be neglected. Simulations indicate that the longitudinal head-tail instability can be controlled by not allowing η_2/η_1 to become too large. Detailed studies of the acceptable parameter ranges are underway.

BNS Damping

Since the synchrotron radiation radiation damping is negligible and the ring is quasi-isochronous (so that the effect of Landau damping is very small), neither of these are likely to may damp collective instabilities. "External" mechanisms, such as BNS damping, may be needed to stabilize the system. The BNS damping can be achieved by a radio frequency quadrupole (RFQ), which introduces a betatron tune spread across the bunch such that the bunch tail experiences a larger betatron focusing than the bunch head [17]. Fig. (8.23) shows that the BBU-like instability is stabilized when a small BNS tune spread is applied to the beam. One should note that, the BNS damping works for the ring only when the potential-well distortion is compensated by rf phase offset, such that the bunch shape remains approximately stationary. This is because the amount of BNS tune spread obtained from the prescribed formula $\triangle\nu_\beta(z)/\nu_\beta = \Upsilon(z)/\pi\nu_\beta$, involves the bunch's density profile. To maintain the correct BNS detuning condition, the bunch shape should not seriously deviate from its initial state; otherwise, one needs to adjust the BNS tune spread accordingly. Investigations are underway to determine if such an rf quadrupole is feasible. In addition, the transverse chromaticity, which causes betatron tune spread, may provide some Landau damping of the instability.

Conclusions

Various single bunch collective effects have been examined. The longitudinal microwave instability is, at present, seen to be the greatest threat to maintaining the bunch length. Operation at $\eta_1 = 10^{-7}$ is being considered, along with ideas for compensating the energy variation induced by the longitudinal wake. The transverse strong head-tail instability with the small η is seen to be BBU-like and can be stabilized by BNS damping. Other instabilities are not believed to be severe over the short storage times.

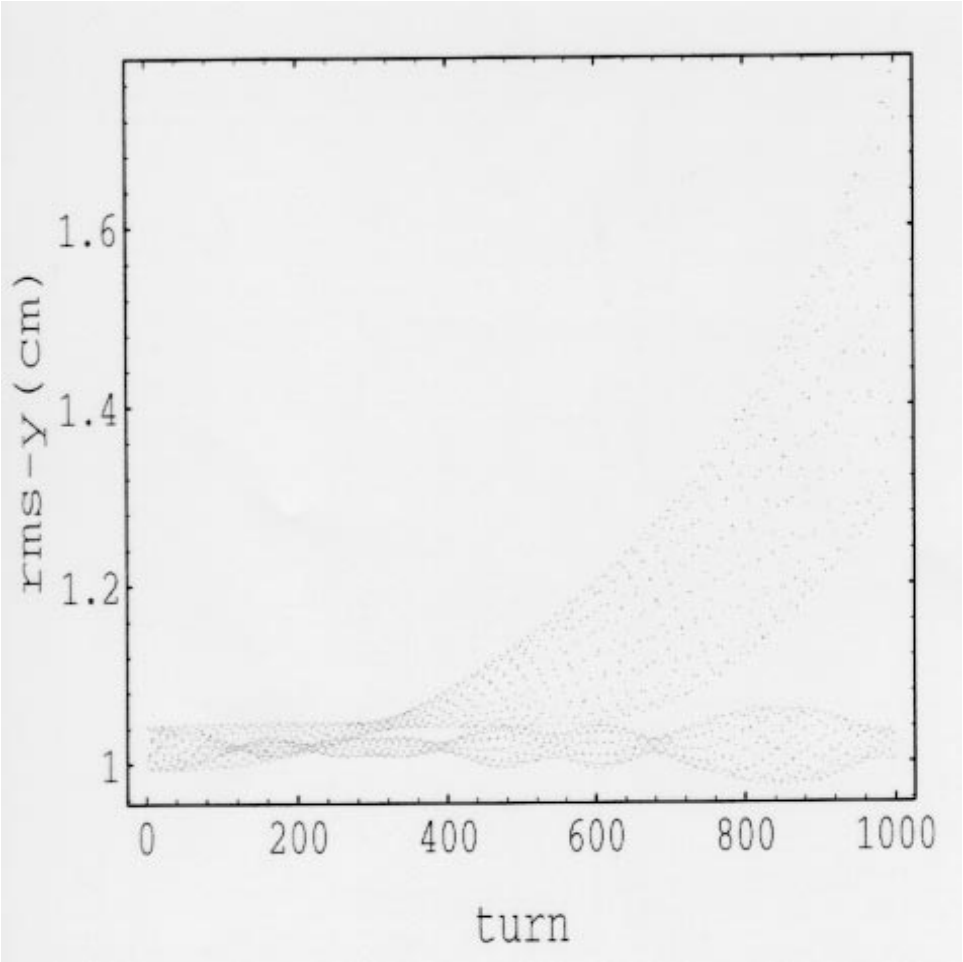

Figure 8.23: Blow up of the rms beam size, due to the BBU-like effect, where $1/\nu_s = 1784$. Note that $R_s/Q = 18225(\Omega)$, $b_{cavity} = 1.3$cm are used for the resonator model, injection error $\Delta y = 0.2$cm, and $\Upsilon(1\sigma_z) \simeq 0.017$. After BNS damping is applied, $\triangle\nu_\beta(1\sigma_z)/\nu_\beta \simeq 6 \times 10^{-5}$, the beam size fluctuates only slightly around 1 cm, a nominal injection beamsize.

Bibliography

[1] A. Garren, et al., *Design of the Muon Collider Lattice: Present Status*, to appear in Proc. of the San Fransisco Workshop on the Physics of Muon Colliders, 1996.

[2] N.M. Gelfand, *A Prototype Lattice Design for a 2 TeV $\mu^+\mu^-$ Collider*, Fermilab Report TM-1933, 1995; King-Yuen Ng, presentation at the 9th Advanced ICFA Beam Dynamics Workshop, Montauk, New York, Nov. 1995; D. Trbojevic, et al., *Design of the Muon Collider Isochronous Storage Ring Lattice*, Proceedings of the Micro Bunches Workshop, Eds. E. Blum, M. Dienes and J. Murphy, Conference Proceedings 367 (1996) ; C. Johnstone and K.-Y. Ng, *Interaction Regions for a Muon Collider* , ibid.

[3] Juan C. Gallardo and Robert B. Palmer, *Final Focus System for a Muon Collider A Test Model*, to appear in Proc. of the San Fransisco Workshop on the Physics of Muon Colliders, 1996.

[4] S. Y. Lee, K. Y. Ng and D. Trbojevic, *Minimizing dispersion in flexible-momentum-compaction lattices*, Phys. Rev. E **48**, 3040 (1993)

[5] R. B. Palmer, *Beam Dynamics in a Muon Collider* Beam Dynamics Newsletter, No.8 (1994) 27, Eds. K. Hirata, S. Y. Lee and F. Willeke.

[6] F. Zimmermann, et al., *A Final Focus System for the Next Linear Collider*, SLAC-PUB-95-6789, June 1995, presented at PAC95, Dallas, Texas, May 1-5, 1995; to be published; O. Napoly, *CLIC Final Focus System: Upgraded version with increased bandwidth and error analysis*, DAPNIA/SEA 94 10, CLIC Note 227, 1994.

[7] K. Brown, *A conceptual Design of Final Focus Systems for Linear Colliders*, SLAC-PUB-4159, (1987).

[8] R. Brinkmann, *Optimization of a Final Focus System for Large Momentum Bandwidth*, DESY-M-90-14, 1990.

[9] K. Johnsen, *Effects of Nonlinearities on Phase Transition*, Proc. CERN Symposium on High Energy Accelerators and Pion Physics, Geneva, Vol.**1**, 106 (1956).

[10] K.Y. Ng, *Higher-Order Momentum Compaction for a Simplified FODO Lattice and Comparison with SYNCH*, Fermilab Internal Report FN-578, 1991.

[11] L. Schachinger, private communication.

[12] N. V. Mokhov, "The MARS Code System User's Guide, version 13 (95)", FNAL–FN–628 (1995).

[13] N. V. Mokhov and S. I. Striganov, *Simulation of Backgrounds in Detectors and Energy Deposition in Superconducting Magnets at $\mu^+\mu^-$ Colliders*, Proc. of the 9th Advanced ICFA Beam Dynamics Workshop, Ed. J C. Gallardo, Conference Proceedings 372 (1996); also Fermilab–Conf–96/011 (1996).

[14] Perry Wilson, SLAC, private communication).

[15] Perry Wilson, SLAC-PUB-2884 (Rev.), "High Energy Electron Linacs", 1991, p. 77)

[16] A. Mosnier, DAPNIA-SEA-92-06, CE Saclay.

[17] Alex Chao, "Physics of Collective Beam Instabilities in High Energy Accelerators", Eqn. 2.194, p. 118.

[18] A. Mathewson, E. Alge, O. Grobner, R. Souchet and P. Strubin, J. Vac. Sci. Technol. A5, 2512 (1987).

[19] A. Mathewson, C. Reymermier and S. Zhang, CERN Vac. Tech. Note 95-22 (1995).

[20] M. Furman, *The Classical Beam-Beam Interaction for the Muon Collider: a First Look* , BF-19/CBP-Note-169/LBL-38563, April 1996.

[21] D. Rice, *Observations of the Beam-Beam Effect in PEP, SPEAR and CESR*, Proc. Third Advanced ICFA Beam Dynamics Workshop (Beam-Beam Effects in Circular Colliders), I. Koop and G. Tumaikin, eds., Novosibirsk, May 29–June 3, 1989, p. 17.

[22] S. Krishnagopal and R. Siemann, *Coherent Beam-Beam Interaction in Electron-Positron Colliders*, Phys. Rev. Lett. **67**, pp. 2461–2464 (1991).

[23] R. Siemann, *The Beam-Beam Interaction in e^+e^- Storage Rings*, SLAC-PUB-6073, March 1993; Proc. Joint US-CERN School on Particle Accelerators: *Frontiers of Particle*

Beams, Factories with e^+e^- rings, Benalmádena, Spain, October, 1992, pp. 327–363 (Springer Verlag Lecture Notes in Physics no. 425, M. Dienes, M. Month, B. Strasser and S. Turner, eds.).

[24] J. L. Tennyson, undocumented code *TRS*, 1989.

[25] M. A. Furman, *Beam-Beam Issues in Asymmetric Colliders*, LBL-32561/UC-414/ESG-205/ABC-77, July 1992, invited talk presented at the Conference on B Factories: The State of the Art in Accelerators, Detectors and Physics, Stanford, CA, April 6–10, 1992 (proceedings, p. 109); invited talk presented at the Washington APS Meeting, Washington, DC, April 18–23, 1992.

[26] R. H. Siemann, private communication.

[27] D. Shatilov and A. Zholents, *Lifetime and Tail Simulations for Beam-Beam Effects in PEP-II B Factory*, to be published in the Proc. 1995 Particle Accelerator Conference and International Conference on High Energy Accelerators (Dallas, Texas, May 1–6, 1995); LBL-36484.

[28] J. Irwin, *Simulation of Tail Distributions in Electron-Positron Circular Colliders*, SLAC-PUB-5743, February 1992; Proc. Third Advanced ICFA Beam Dynamics Workshop (Beam-Beam Effects in Circular Colliders), I. Koop and G. Tumaikin, eds., Novosibirsk, May 29–June 3, 1989, p. 123.

[29] T. Chen, J. Irwin and R. Siemann, *Simulation of the Beam Halo from the Beam-Beam Interaction*, SLAC-PUB-6379, October, 1993; Phys. Rev. **E49**, March 1994, p. 2323.

[30] This is an old subject; a relatively recent reference is: M. A. Furman, *Hourglass Effects for Asymmetric Colliders*, LBL-30833, Proc. 1991 Particle Accelerator Conf., San Francisco, May 6–9, 1991, p. 422.

[31] R.B. Palmer. Beam Dynamics Newsletter. # 8 (1995); Report at 3-rd Int. Conf. *Physics Potential & Developments of $\mu^+\mu^-$ Colliders*, San Francisco, December 13–15, 1995.

[32] I. Ginzburg, *The e^+e^- pair production at $\mu^+\mu^-$ collider.*, submitted for publication.

[33] L.D. Landau, E.M. Lifshitz. Phys. Zs. Sovjet **6** (1934) 244.

[34] V.M. Budnev, I.F. Ginzburg, G.V. Meledin and V.G. Serbo. Phys.Rep. **15C** (1975) 181.

[35] V.M. Budnev, I.F. Ginzburg, G.V. Meledin, V.G. Serbo. Phys. Lett. **39B** (1972) 526; Nucl.Phys. **B63** (1973) 519.

[36] C. Racah. Nuovo Cim. **14** (1937) 93.

[37] R.B. Palmer. Private communication.

[38] A.I. Nikishov, V.I. Ritus. Sov. ZhETF **46** (1964) 776.

[39] K.Y. Ng, *Beam Stability Issues in a Quasi-Isochronous Muon Collider*, Proceedings of the 9th Advanced ICFA Beam Dynamics Workshop, Ed. J. C. Gallardo, AIP Press, Conference Proceedings 372 (1996).

[40] W. H. Cheng, A. M. Sessler, and J. S. Wurtele, *Studies of Collective Instabilities, in Muon Collider Rings*, Proceedings of the 9th Advanced ICFA Beam Dynamics Workshop, Ed. J.C. Gallardo, AIP Press, to be published.

[41] C. Pellegrini, Nuovo Cimento 64A, 447 (1969). B. Chen and A. W. Chao, Particle Accelerators, vol. 43(1-2), pp77-91,1993.

[42] W.-H.Cheng, A.M. Sessler and J.S. Wurtele, "Alternating chromaticity: a damping mechanism for the transverse head-tail instability", in prepariation.

Contributors

- J. S. Wurtele, (Univ. California Berkeley) Editor
- W-H Cheng (LBNL)
- E. Courant (BNL)
- M. Furman (LBNL)
- J. Gallardo (BNL)
- A. Garren (LBNL)
- I. Ginzburg (Inst. of Math., Novosibirsk)
- M. Green (LBNL)
- C. Johnstone (FermiLab)
- N. Mokhov (FermiLab)
- K-Y. Ng (FermiLab)
- K. Oide (KEK)
- R. Palmer (BNL)
- J. Peterson (LBNL)
- A. M.Sessler (LBNL)
- D. Trbojevic (BNL)
- W. Turner (LBNL)
- E. Willen (BNL)

List of Figures

8.1 The complete collider ring layout. 329
8.2 Betatron (β_x solid-line; β_y dash-line) and dispersion (dot-line) functions of an arc-module. 331
8.3 Betatron (β_x solid-line; β_y dash-line) and dispersion (dot-line) functions of a dispersion suppressor module. 332
8.4 Experimental insert (half) with extremely small beta function at the IP. . . . 333
8.5 Utility insertion (half) 334
8.6 Fractional tunes $Q_{x,y}$ vs $\frac{\Delta p}{p}$ 335
8.7 Beta function β^* vs $\frac{\Delta p}{p}$ 335
8.8 Chromaticity vs $\frac{\Delta p}{p}$ 336
8.9 Momentum compaction α vs $\frac{\Delta p}{p}$ 336
8.10 Amplitude dependent tune shift $\frac{dQ}{d\epsilon}$ vs $\frac{\Delta p}{p}$ 337
8.11 A cold iron 8.5 T cosine theta dipole with a 65 mm thick tungsten liner at 300 K 343
8.12 Two versions of an 8.5 T cold iron split dipole that would have less than 0.1% of the muon decay power deposited within the superconducting coils 344
8.13 A quadrupole design that avoids superconductor on the midplane 345
8.14 Azimuthal distribution of power density in the first SC cable shell in the collider arc for different tungsten liners inside the aperture for 2 TeV muon beam decays 346
8.15 Maximum and azimuthal averaged power density in the first SC cable shell in the collider arc *vs* tungsten liner thickness for 2 TeV muon beam decays. . . 347
8.16 Power dissipation in the arc magnet components *vs* tungsten liner thickness for 2 TeV muon beam decays. 348
8.17 Luminosity as a function of turn number assuming that the muons are stable particles 360
8.18 Luminosity as a function of turn number, taking into account the finite muon lifetime 361

8.19 Luminosity as a function of turn number for three different values of the number of particles per bunch N 362
8.20 The hourglass luminosity reduction factor when the collisions are longitudinally displaced from the IP by a distance s_c, plotted as a function of s_c/σ_z . 365
8.21 Scaled rms bunch size and rms energy-spread vs. turn 372
8.22 Center of energy-spread vs. center of bunch size 373
8.23 Blow up of the rms beam size, due to the BBU-like effect, where $1/\nu_s = 1784$ 375

List of Tables

8.1 High energy-high luminosity $\mu^+ \mu^-$ collider 328
8.2 Muon decay parameters for various parts of a muon collider 342
8.3 Collider parameters used for the rf system 348
8.4 Time average $\mu^{\pm}$ particle fluxes, characteristic energies and power incident on the beam tube 352
8.5 Characteristic apertures and rms beam dimensions in the collider ring. Note that $\epsilon = \sigma^2/\beta = 2.65 \times 10^{-9} m - rad$ 354
8.6 Estimated sources of gas and average partial pressures in the collider beam tube. 355
8.7 Resistive wall dissipation for Cu, Al and SS beam tubes. 355
8.8 Muon collider parameters. 358